arXiv:2101.10010v1 [astro-ph.HE] 25 Jan 2021

First *Fermi*-LAT Solar flare catalog

M. Ajello[1], L. Baldini[2], D. Bastieri[3,4], R. Bellazzini[5], A. Berretta[6], E. Bissaldi[7,8], R. D. Blandford[9], R. Bonino[10,11], P. Bruel[12], S. Buson[56] R. A. Cameron[9], R. Caputo[13], E. Cavazzuti[14], C. C. Cheung[15], G. Chiaro[16], D. Costantin[17], S. Cutini[18], F. D'Ammando[19], F. de Palma[10], R. Desiante[10], N. Di Lalla[9], L. Di Venere[7,8], F. Fana Dirirsa[20], S. J. Fegan[12], Y. Fukazawa[21], S. Funk[22], P. Fusco[7,8], F. Gargano[8], D. Gasparrini[23,24], F. Giordano[7,8], M. Giroletti[19], D. Green[25], S. Guiriec[26,13], E. Hays[13], J.W. Hewitt[27], D. Horan[12], G. Jóhannesson[28,29], M. Kovac'evic'[18], M. Kuss[5], S. Larsson[30,31,32], L. Latronico[10], J. Li[33], F. Longo[34,35,36], M. N. Lovellette[15], P. Lubrano[18], S. Maldera[10], A. Manfreda[2], G. Martí-Devesa[37], M. N. Mazziotta[8], I.Mereu[6,18], P. F. Michelson[9], T. Mizuno[38], M. E. Monzani[9], A. Morselli[23], I. V. Moskalenko[9], M. Negro[39,40], N. Omodei[9,41], M. Orienti[19], E. Orlando[42,9], D. Paneque[25], Z. Pei[4], M. Persic[34,43], M. Pesce-Rollins[5,44], V. Petrosian[9,45], F. Piron[46], T. A. Porter[9], G. Principe[19], J. L. Racusin[13], S. Rainò[7,8], R. Rando[47,3,48], B. Rani[49,13], M. Razzano[5,50], S. Razzaque[20], A. Reimer[37,9], O. Reimer[37], D. Serini[7], C. Sgrò[5], E. J. Siskind[51], G. Spandre[5], P. Spinelli[7,8], D. Tak[52,13], E. Troja[13,53], J. Valverde[12], K. Wood[54], G. Zaharijas[42,55]

[1]Department of Physics and Astronomy, Clemson University, Kinard Lab of Physics, Clemson, SC 29634-0978, USA

[2]Università di Pisa and Istituto Nazionale di Fisica Nucleare, Sezione di Pisa I-56127 Pisa, Italy

[3]Istituto Nazionale di Fisica Nucleare, Sezione di Padova, I-35131 Padova, Italy

[4]Dipartimento di Fisica e Astronomia "G. Galilei", Università di Padova, I-35131 Padova, Italy

[5]Istituto Nazionale di Fisica Nucleare, Sezione di Pisa, I-56127 Pisa, Italy

[6]Dipartimento di Fisica, Università degli Studi di Perugia, I-06123 Perugia, Italy

[7]Dipartimento di Fisica "M. Merlin" dell'Università e del Politecnico di Bari, via Amendola 173, I-70126 Bari, Italy

[8]Istituto Nazionale di Fisica Nucleare, Sezione di Bari, I-70126 Bari, Italy

[9]W. W. Hansen Experimental Physics Laboratory, Kavli Institute for Particle Astrophysics and Cosmology, Department of Physics and SLAC National Accelerator Laboratory, Stanford University, Stanford, CA 94305, USA

[10]Istituto Nazionale di Fisica Nucleare, Sezione di Torino, I-10125 Torino, Italy

[11]Dipartimento di Fisica, Università degli Studi di Torino, I-10125 Torino, Italy

[12]Laboratoire Leprince-Ringuet, École polytechnique, CNRS/IN2P3, F-91128 Palaiseau, France

[13]NASA Goddard Space Flight Center, Greenbelt, MD 20771, USA

[14]Italian Space Agency, Via del Politecnico snc, 00133 Roma, Italy

[15]Space Science Division, Naval Research Laboratory, Washington, DC 20375-5352, USA

[16]INAF-Istituto di Astrofisica Spaziale e Fisica Cosmica Milano, via E. Bassini 15, I-20133 Milano, Italy

[17]University of Padua, Department of Statistical Science, Via 8 Febbraio, 2, 35122 Padova

[18]Istituto Nazionale di Fisica Nucleare, Sezione di Perugia, I-06123 Perugia, Italy

[19]INAF Istituto di Radioastronomia, I-40129 Bologna, Italy

[20]Department of Physics, University of Johannesburg, PO Box 524, Auckland Park 2006, South Africa

[21]Department of Physical Sciences, Hiroshima University, Higashi-Hiroshima, Hiroshima 739-8526, Japan

[22]Friedrich-Alexander Universität Erlangen-Nürnberg, Erlangen Centre for Astroparticle Physics, Erwin-Rommel-Str. 1, 91058 Erlangen, Germany

[23]Istituto Nazionale di Fisica Nucleare, Sezione di Roma "Tor Vergata", I-00133 Roma, Italy

[24]Space Science Data Center - Agenzia Spaziale Italiana, Via del Politecnico, snc, I-00133, Roma, Italy

[25]Max-Planck-Institut für Physik, D-80805 München, Germany

[26]The George Washington University, Department of Physics, 725 21st St, NW, Washington, DC 20052, USA

[27]University of North Florida, Department of Physics, 1 UNF Drive, Jacksonville, FL 32224 , USA

[28]Science Institute, University of Iceland, IS-107 Reykjavik, Iceland

[29]Nordita, Royal Institute of Technology and Stockholm University, Roslagstullsbacken 23, SE-106 91 Stockholm, Sweden

[30]Department of Physics, KTH Royal Institute of Technology, AlbaNova, SE-106 91 Stockholm, Sweden

[31]The Oskar Klein Centre for Cosmoparticle Physics, AlbaNova, SE-106 91 Stockholm, Sweden

[32]School of Education, Health and Social Studies, Natural Science, Dalarna University, SE-791 88 Falun, Sweden

[33]Deutsches Elektronen Synchrotron DESY, D-15738 Zeuthen, Germany

[34]Istituto Nazionale di Fisica Nucleare, Sezione di Trieste, I-34127 Trieste, Italy

[35]Dipartimento di Fisica, Università di Trieste, I-34127 Trieste, Italy

[36]email: francesco.longo@trieste.infn.it

[37]Institut für Astro- und Teilchenphysik, Leopold-Franzens-Universität Innsbruck, A-6020 Innsbruck, Austria

[38]Hiroshima Astrophysical Science Center, Hiroshima University, Higashi-Hiroshima, Hiroshima 739-8526, Japan

[39]Center for Research and Exploration in Space Science and Technology (CRESST) and NASA Goddard Space Flight Center, Greenbelt, MD 20771, USA

[40]Department of Physics and Center for Space Sciences and Technology, University of Maryland Baltimore County, Baltimore, MD 21250, USA

[41]email: nicola.omodei@stanford.edu

[42]Istituto Nazionale di Fisica Nucleare, Sezione di Trieste, and Università di Trieste, I-34127 Trieste, Italy

[43]Osservatorio Astronomico di Trieste, Istituto Nazionale di Astrofisica, I-34143 Trieste, Italy

[44]email: melissa.pesce.rollins@pi.infn.it

[45]email: vahep@stanford.edu

[46]Laboratoire Univers et Particules de Montpellier, Université Montpellier, CNRS/IN2P3, F-34095 Montpellier, France

[47]Department of Physics and Astronomy, University of Padova, Vicolo Osservatorio 3, I-35122 Padova, Italy

[48]Center for Space Studies and Activities "G. Colombo", University of Padova, Via Venezia 15, I-35131 Padova, Italy

[49]Korea Astronomy and Space Science Institute, 776 Daedeokdae-ro, Yuseong-gu, Daejeon

Received _____; accepted _____

30455, Korea

[50]Funded by contract FIRB-2012-RBFR12PM1F from the Italian Ministry of Education, University and Research (MIUR)

[51]NYCB Real-Time Computing Inc., Lattingtown, NY 11560-1025, USA

[52]Department of Physics, University of Maryland, College Park, MD 20742, USA

[53]Department of Astronomy, University of Maryland, College Park, MD 20742, USA

[54]Praxis Inc., Alexandria, VA 22303, resident at Naval Research Laboratory, Washington, DC 20375, USA

[55]Center for Astrophysics and Cosmology, University of Nova Gorica, Nova Gorica, Slovenia

[56]Institut für Theoretische Physik und Astrophysik, Universität Würzburg, Campus Hubland Nord Emil-Fischer-Str. 31 97074 Würzburg, Germany

ABSTRACT

We present the first *Fermi*-Large Area Telescope (LAT) solar flare catalog covering the 24^{th} solar cycle. This catalog contains 45 *Fermi*-LAT solar flares (FLSFs) with emission in the γ-ray energy band (30 MeV - 10 GeV) detected with a significance $\geq 5\sigma$ over the years 2010-2018. A subsample containing 37 of these flares exhibit delayed emission beyond the prompt-impulsive hard X-ray phase with 21 flares showing delayed emission lasting more than two hours. No prompt-impulsive emission is detected in four of these flares. We also present in this catalog the observations of GeV emission from 3 flares originating from Active Regions located behind the limb (BTL) of the visible solar disk. We report the light curves, spectra, best proton index and localization (when possible) for all the FLSFs. The γ-ray spectra is consistent with the decay of pions produced by >300 MeV protons. This work contains the largest sample of high-energy γ-ray flares ever reported and provides the unique opportunity to perform population studies on the different phases of the flare and thus allowing to open a new window in solar physics.

1. Introduction

It is generally accepted that the magnetic energy released through reconnection during solar flares is capable of accelerating electrons and ions to relativistic energies on time scales as short as a few seconds. Much is known of the electron acceleration during these explosive phenomena thanks to the observations made in Hard X-rays (10 keV - 1 MeV; HXRs; (see, e.g. Vilmer 1987; Dennis 1988; Lin & Rhessi Team 2003) and microwaves (see, e.g. Trottet et al. 1998). The observed impulsive phase radiation in solar flares is dominated by electron emission, however a fair fraction of stronger flares, with longer impulsive phase, show even higher-energy emission at γ-ray energies ($E > 3$ MeV) by accelerated protons and other ions in the form of nuclear de-excitation lines, by ∼3 - 50 MeV ions, and >100 MeV continuum

due to decay of pions produced by > 300 MeV ions (see, e.g. Vilmer et al. 2011). The first reported observation of γ-rays with energies above 10 MeV was made in 1981 with the Solar Maximum Mission (SMM) spectrometer (Chupp et al. 1982) and throughout the 1980's several other observations were made (see, e.g. Forrest et al. 1985, 1986) providing evidence of pion-decay emission and revealing multiple phases in the flares.

The first detection of GeV γ-rays were made by the *Energetic Gamma-Ray Experiment Telescope* (EGRET) on board the *Compton Gamma-Ray Observatory* (CGRO) (see, e.g. Kanbach et al. 1993; Vilmer et al. 2003). The majority of the flares observed from 50 MeV to 2 GeV by EGRET had durations lasting tens of minutes but up to several hours in two flares leading to a new class of flares initially known as *Long Duration Gamma-Ray Flares* (Ryan 2000; Chupp & Ryan 2009). This new class of flares presented a challenge to the *classical* magnetic reconnection theory for particle acceleration during flares because the γ-ray emission persisted beyond any other flare emissions, therefore suggesting the need for an additional mechanism and site for acceleration of protons and other ions. However, with only two such detections the search for an additional acceleration mechanism and site was very challenging.

Additional cases suggesting the need for a new source of ion acceleration came with the observations of γ-ray emission, up to only 100 MeV, from three flares whose host Active Regions (ARs) were located behind the limb (BTL) of the visible solar disk (Vestrand & Forrest 1993; Vilmer et al. 1999; Barat et al. 1994). It is generally believed that the lower energy γ-rays are produced at the dense footpoints of flare loops by ions accelerated at the reconnection regions near the top of these loops. Thus, observations of BTL flares pose interesting questions regarding the acceleration site and mechanism, of the ions and about their transport to the high density photospheric regions on the visible disk. Although there were some scenarios put forth (Cliver et al. 1993), no convincing explanations were given for the acceleration and transport sites and mechanisms of particles responsible for these observations.

Prior to the launch of the *Fermi* Gamma-ray Space Telescope in 2008, the

understanding of these emission mechanisms was severely limited because of the limited amount of high-energy γ-ray flares detected.

The *Fermi*-Large Area Telescope (LAT, Atwood et al. 2009) observations of the flaring Sun over the first 12 years in orbit have revealed an extremely rich and diverse sample of events, spanning from short prompt-impulsive flares (Ackermann et al. 2012a) to the gradual-delayed long-duration phases (Ackermann et al. 2014a) including the longest extended emission ever detected ($\sim$20 hours) from the SOL2012-03-07; a GOES X-class flare (Ajello et al. 2014)[1]. The LAT, thanks to its large field of view (FoV) of 2.4 sr, monitors the entire sky every two orbits as an excellent general purpose γ-ray astrophysics observatory but in doing so it keeps the Sun in the FoV 40% of the time.

Nonetheless, thanks to its technology improvements with respect to previous γ-ray space based missions, the *Fermi*-LAT has increased the total number of >30 MeV detected solar flares by almost a factor of 10. More importantly the LAT with its higher spatial resolution than EGRET can localize the centroids of the γ-ray emissions on the photosphere, which is particulary important for the interpretation of the BTL flares.

In this *Fermi*-LAT Solar Flare (FLSF) catalog we present the observations of 45 flares with >30 MeV emission in the period January 2010 - January 2018 (covering most of the $24^{\rm th}$ solar cycle). From these observations we now know that >100 MeV γ-ray emission from even moderate GOES class flares is fairly common (roughly half of the FLSFs in our catalog are associated with M class flares) and that this high-energy emission is not correlated with the intensity of the X-ray flare, as one might expect. Our spectral analysis indicates that the >100 MeV emission is due to accelerated ions as opposed to HXR and microwave producing electrons. Based on the timing evolution of the γ-ray emission we find that there are two main populations of γ-ray flares: impulsive-prompt (prompt

[1]Solar flares observed by the Geostationary Operational Environmental Satellite (GOES) are classified, on the basis of their peak flux in the soft X-ray range of 0.5 to 10 keV, as X, M, C and A class with peak fluxes greater than $10^{-4}, 10^{-5}, 10^{-6}$ and 10^{-7} Watt m^{-2}, respectively

hereafter) and gradual-delayed (delayed hereafter). The prompt flares are those whose emission evolution is similar to that of the HXRs, indicating common acceleration sites and mechanism of electrons and ions. The emission of delayed FLSF flares, which are always (with the exception of FLSF 2012-10-23 and FLSF 2012-11-27) associated with fast Coronal Mass Ejections (CMEs), rises at the end of the impulsive HXR phase and, like Solar Energetic Particles (SEPs), extends well beyond the end of the HXR emission (for up to tens of hours). This and other observations suggest a different acceleration site and mechanism.

In section 2 we describe the analysis methods and procedures used in this work, which includes the description of an automated pipeline (2.1), the LAT Low Energy (LLE) analysis (2.2), spectral analysis (2.3), how we perform our localization of the γ-ray emission (2.4), and the search for spatial extension in the γ-ray emission of the brightest flares (2.5). Here we also describe the methods used to calculate the total emission, fluence and the total number of accelerated >500 MeV protons needed to produce the observed emission (2.6). In section 3 we describe how the solar flares are classified based on the evolution of their γ-ray emission. In section 4 we present the results of the catalog. In section 5 we discuss the main findings of this work and the theoretical implications of our results. The tables and figures for each individual flare in this catalog are reported in Ajello et al. (2020).

2. Analysis methods and procedures

The LAT is sensitive to γ-rays in the energy range between 30 MeV and >300 GeV (Atwood et al. 2013). The LAT registers energy, direction and time information for each detected particle. Each such "event" is classified by on-ground processing as a photon or other particle based on the consistency of its interaction with those expected from energetic γ rays.

Event classes correspond to different levels of purity tolerance of the γ-ray sample appropriate for use in different types of analyses. For each event class there is a

corresponding set of Instrument Response Functions (IRFs) describing the performance of the instrument. The standard analysis and software are described at the *Fermi* Science Support Center (FSSC) web site[2] and, in great detail, in Ackermann et al. (2012b).

For the FLSF catalog we developed two analysis chains, the first one, that we call *standard*, uses data with energies between 60 MeV and 10 GeV from two sets of event classes, `P8R3_SOURCE` and the solar flare Transient class `P8R3_TRANSIENT015s` (S15)[3]. The `P8R3_SOURCE`(Bruel et al. 2018) class is the event class recommended for the standard *Fermi*-LAT source analysis, while the S15 class was specifically developed to be insensitive to the potential pulse pile-up in the anti-coincidence detector (ACD) scintillators of the LAT resulting from the intense flux of X-rays during the prompt phase of solar flares. Pile-up of X-rays during the readout integration time of the ACD coincident with the entry of a γ-ray into the LAT can cause the otherwise good γ-ray to be misidentified as a charge particle by the instrument flight software or event-classification ground software and thereby mistakenly vetoed. The *Fermi*-LAT instrument team closely monitors this effect and tags time intervals with particularly high activity in the sunward ACD tiles as "bad time intervals" (BTI) in the public data archive[4]. The S15 event class is robust against these spurious vetoes because it is defined using selections that exclude variables associated with the Anti-Coincidence Detector and are therefore less susceptible to X-ray pile-up activity which can occur during the impulsive phase of solar flares; thus all analysis in this catalog during a BTI used the S15 event class.

Additionally, a subset of results on short duration prompt solar flares was obtained using the second chain based on LLE analysis methods. The LLE technique is an analysis method designed to study bright transient phenomena, such as Gamma Ray Bursts and solar flares, in the 30 MeV–1 GeV energy range. The LAT collaboration developed this

[2]`http://fermi.gsfc.nasa.gov/ssc/`

[3]Events belonging to the `P8R_TRANSIENT015s` class are available in the extended photon data through the *Fermi* Science Support Center

[4]`http://fermi.gsfc.nasa.gov/ssc/data/access/`

analysis using a different approach from that used in the standard photon analysis. The idea behind LLE is to maximize the effective area below ~ 1 GeV by relaxing the standard analysis requirement on background rejection; see Ajello et al. (2014) for a full description of the LLE method. The LAT collaboration has already used the LLE technique to analyze solar flares, in particular FLSF 2010-06-12 (the first flare detected by the LAT, see Ackermann et al. 2012a) and the prompt phase of the FLSF 2012-03-07 flares (Ajello et al. 2014). In this FLSF catalog we used the LLE selection to study the short prompt phase of 14 solar flares.

These two approaches are complementary: the LLE method suffers from large background contamination and is effective only for short transients but, because it is much less restrictive than the `P8R3_SOURCE` event class, the LLE class has much larger effective area and has significantly greater sensitivity at high incidence angles.

Indeed, the FLSF 2010-06-12 was detected with the LLE approach when the Sun was more than 75° off-axis (Ackermann et al. 2012a).

2.1. The *Fermi*-LAT `SunMonitor`

We have created an automated data analysis pipeline, the *Fermi*-LAT `SunMonitor`, to monitor the high-energy γ-ray flux from the Sun throughout the *Fermi* mission. [5] The time intervals during which we run the analysis are when the Sun is $< 70°$ from the LAT boresight.

The effective area of the LAT decreases significantly for sources at incidence angles larger than 60°, so only very bright transients are detectable past this limit. Selecting a maximum off-axis angle of 70° extends the window of continuous Sun exposure for the brightest flares. The duration of these windows vary (ranging from 5 to 80 minutes, with an average duration of 30 minutes, as is shown in Figure 1) as the Sun advances along

[5]Results from this pipeline are available online at `https://hesperia.gsfc.nasa.gov/fermi_solar/`.

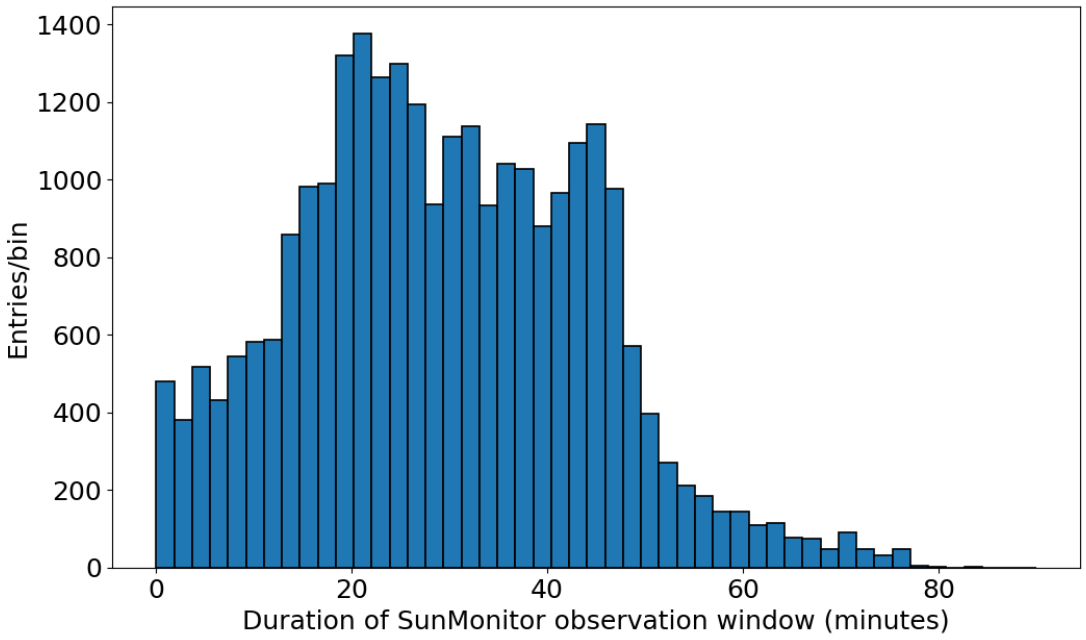

Fig. 1.— Duration of the *Fermi* `SunMonitor` observation windows. The duration varies from 5 to 80 minutes with an average duration of 30 minutes.

the ecliptic and as the orbit of *Fermi* precesses. Contamination from γ rays produced by cosmic-ray interactions with the Earth's atmosphere is reduced by selecting only events arriving within 100° of the zenith[6].

Each interval is analyzed using a Region of Interest (RoI) of 10° radius, centered on the position of the Sun at the central time of the interval. On average the duration of a `SunMonitor` interval is 30 minutes. During this time, the maximum deviation of the true position of the Sun from the RoI center due to its apparent motion is $\sim 0.^{\circ}02$. This is smaller than the typical angular resolution of the instrument: the 68% containment angle of the reconstructed incoming γ-ray direction for normal incidence at 1 GeV is $0.^{\circ}8$ and at 100 MeV is 5°. Furthermore, the statistical uncertainty on the measured centroid of the >100 MeV emission is always larger than $0.^{\circ}03$, even for the brightest solar flares. It is therefore not necessary to apply a correction to account for the motion of the Sun from the center of the RoI. In each `SunMonitor` interval we perform an unbinned maximum likelihood analysis using the tools in the *Fermi* ScienceTools software package[7]. The unbinned analysis computes the log-likelihood of the data using the reconstructed direction and energy of each individual γ-ray and the assumed sky model folded through the instrument response functions corresponding to the selected event class.

The likelihood analysis consists of maximizing the probability of obtaining the data given an input model as well as deriving error estimates. The RoI is modeled with a solar component and two templates for diffuse γ-ray background emission: a galactic component produced by the interaction of cosmic rays with the gas and interstellar radiation fields of the Milky Way, and an isotropic component that includes both the contribution of the extragalactic diffuse emission and the residual cosmic rays that passed

[6]We used the `gtmktime` filter cut = `(DATA_QUAL>0||DATA_QUAL==-1) LAT_CONFIG==1 angsep(RA_ZENITH,DEC_ZENITH,RA,DEC)< (zmax-rad)` where RA and DEC are those of the postion of the Sun at the time of the flare, zmax= 100° and rad is the radius of the RoI used for the analysis.

[7]We used version 11-05-03 available at `http://fermi.gsfc.nasa.gov/ssc/`

the γ-ray classification[8]. We fix the normalization of the galactic component but leave the normalization of the isotropic background as a free parameter to account for variable fluxes of residual cosmic rays.

When the Sun is not flaring, it is a steady, faint source of γ rays. This emission consists of two components: a disk emission originating from hadronic cosmic-ray cascades in the solar atmosphere and a spatially extended emission from the inverse Compton scattering of cosmic-ray electrons on solar photons in the heliosphere. The disk emission was first mentioned by Dolan & Fazio (1965) and Seckel et al. (1991) and the existence of an additional, spatially extended component was not realized until recently (Moskalenko et al. 2006; Orlando & Strong 2007; Linden et al. 2018; Mazziotta et al. 2020). The quiet Sun was detected for the first time in γ rays in the EGRET data (Orlando & Strong 2008). We also include the quiet Sun emission disk component as a point source in our RoI; however, we did not include the extended Inverse Compton (IC) component described in (Abdo et al. 2011) because it is too faint to be detected during these time intervals. The >100 MeV flux of the solar disk component used in the FLSF catalog, obtained during the first 18 months of *Fermi*-LAT observations (Abdo et al. 2011), is 4.6 $(\pm 0.2^{stat} \pm 1.0^{syst}) \times 10^{-7}$ ph cm^{-2} s^{-1}.

We rely on the likelihood ratio test and the associated test statistic (TS) (Mattox et al. 1996) to estimate the significance of the detection. Here we define TS as twice the increment of the logarithm of the likelihood obtained by fitting the data with the source and background model component simultaneously with respect to a fit with only the background. Note that the significance in σ for the 68% confidence interval can be roughly approximated as $\sqrt{\mathrm{TS}}$.

With a pipeline testing for detection in so many time windows (33511 total over the period of this work), we need to account for the trials factor to understand the statistical significance of a γ-ray source detected in the `SunMonitor` with a particular value of TS.

[8]The models used for this analysis, `gll_iem_v07.fits` and `iso_P8R3_SOURCE_V2_v1.txt`, are available at `http://fermi.gsfc.nasa.gov/ssc/data/access/lat/BackgroundModels.html`

Assuming each window is independent, a TS of 20, which would otherwise correspond to a confidence of about 4.5σ, corresponds to 1.38σ post trials. In order to have a detection significance of $\geq 5\sigma$ we must impose a cut on the TS with a minimum of 30. This corresponds to a selection of 133 time windows, some of them consecutive in time for solar flares lasting more than an hour. Following this systematic sweep with `SunMonitor`, a detailed analysis is performed on those windows with a TS above 30.

From January 2010 to the end of January 2018, we applied the `SunMonitor` pipeline analysis to 33511 intervals of duration longer than 5 minutes. The cases when the duration is less than 5 minutes are likely due to the RoI being close to the maximum zenith angle, or cut short by a passage of the satellite into the South Atlantic Anomaly (SAA). These are generally not long enough to yield a reliable point source likelihood detection and constrain the background. Overall the Sun was observable for an average duty cycle of 28% for the entire timespan of the FLSF catalog.

Note that outside the time interval considered here, since April 2018, the LAT has been operating with a modified observing profile due to a failure of one of the solar array drive assemblies that reduces its exposure to the Sun [9]. This change in observing strategy results in an average 45% reduction in solar exposure for the standard event classes (22% reduction for LLE) and consequently in the potential for solar physics science with the LAT.

2.2. LAT Low Energy Spectral Analysis

The LAT Low Energy (LLE) technique is designed to study bright transient phenomena, such as solar flares, in the 30 MeV–1 GeV energy range. In this catalog we used the LLE selection to study the prompt phase of 14 solar FLSFs. To obtain the LLE spectral data we used the `gtburst` package, available in the Fermitools distribution from the FSSC. The

[9]see: `https://fermi.gsfc.nasa.gov/ssc/observations/types/post_anomaly/` for more information.

LLE data are divided by `gtburst` in 50 logarithmically spaced energy bins from 10 MeV to 10 GeV. For the spectral analysis we used only the bins in the energy range optimised for the LLE selection.

A spectral fit was then performed using the `XSPEC` (Arnaud 1996) package following an approach similar to the one previously adopted for the analysis of the prompt phase of SOL2012-03-07 (Ajello et al. 2014). The results of the joint analysis with *Fermi*-Gamma-ray Burst Monitor (GBM) Bismute-Germanate (BGO) data (300 keV - 20 MeV) will be reported in a forthcoming publication.

2.3. Spectral Analysis

We fit three models to the *Fermi*-LAT γ-ray solar spectral data. The first two, a simple power law (PL) and a power-law with an exponential cut-off (PLEXP), are phenomenological functions that may describe bremsstrahlung emission from relativistic electrons. The parameters of these models are varied to obtain the best fit to the data. When the PLEXP provides a significantly better fit than the PL, we also fit the data with a third model consisting of a pion-decay emission templates[10]. This third model uses a series of γ-ray spectral templates derived from a detailed study of γ rays from the decay of pions produced by interactions of accelerated protons and ions with background protons and ions. The accelerated particles are assumed to have a power-law energy spectrum (dN/dE $\propto$ $E^{-\beta}$), where E is the kinetic energy of the protons with index β and an isotropic pitch angle distribution, injected into a thick target with a coronal composition (Reames 1995) taking He/H = 0.1 (updated from Murphy et al. 1987).

When the PLEXP provides a significantly better fit than the PL, we fit the data with the pion-templates to determine the proton index that best fits the data. To do this, we

[10]We are using only pion-production emission neglecting other (minor) components that contribute to the γ-ray emission

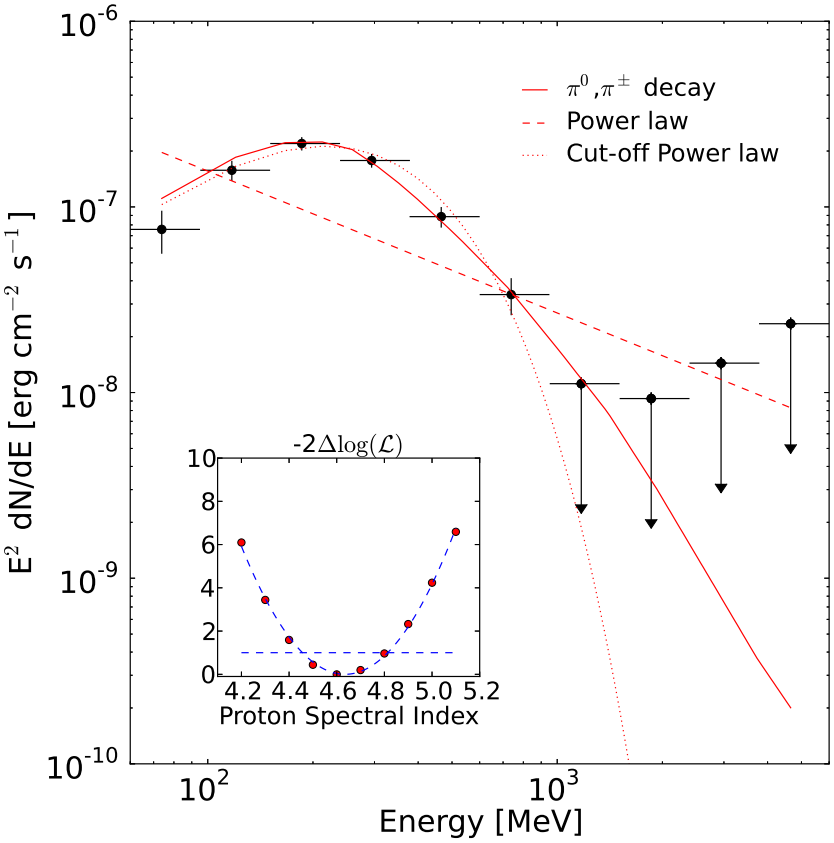

Fig. 2.— Example γ-ray spectra for SOL2012-03-07. The data were fit with three models (PL,PLEXP and pion templates) and when the curved model (PLEXP) is preferred to the PL model we perform a scan over the pion templates to search for the best proton index. In the insert we show the fit to the log-likelihood values with a parabola and the 68% confidence level is indicated by the straight line at $-2\,\Delta\log(\mathcal{L}_{\rm min}) + 1$.

calculate the variation of the log-likelihood with the proton spectral index and fit it with a parabola. We run the likelihood analysis for each of the 41 proton spectral indices available from our templates (2.0 - 6.0 in steps of 0.1). The minimum of this distribution ($\mathcal{L}_{\rm min}$) gives the best fit spectral index, and the corresponding value s_0 as the maximum likelihood. Figure 2 shows an example of a spectral energy distribution of SOL2012-03-07 obtained following this procedure.

Once we have found the proton index corresponding to the best fit and the value of the observed γ-ray emission we can estimate the total number of >500 MeV accelerated protons (N500, hereafter) needed to produce the observed γ-ray emission over a given time following the prescription of Murphy et al. (1987).

To compute the photon spectral energy distribution we divide the data into ten energy bins (in the energy range 60 MeV - 10 GeV) and determine the source flux using the unbinned maximum likelihood algorithm `gtlike` keeping the normalization of the background constant at the best fit value and assuming that the spectrum of the point source is an E^{-2} power law. For non-detections (TS<9), we compute 95% CL upper limits.

2.4. Localizing the emission from *Fermi* LAT Solar Flares

The standard tool to study the localization of γ-ray sources with an unbinned likelihood analysis is the `gtfindsrc` algorithm from the ScienceTools[11]. The likelihood analysis is based on sky models with background sources at fixed spatial positions and the best spectral fit for the source of interest. `gtfindsrc` uses a multidimensional minimization of the unbinned likelihood for a grid of positions around an initial guess until the convergence tolerance for a positional fit is reached. However, the Sun is in the FoV of the LAT for relatively short timescales which can result in inhomogeneous exposure across the FoV. For this reason, we relied on the `gttsmap` algorithm to study the localization for the FLSFs

[11]Available at `http://fermi.gsfc.nasa.gov/ssc/data/analysis/software/`

of the catalog. The TS maps are created by moving a putative point source through a grid of locations on the sky and maximizing -log(likelihood) at each grid point, with any other well-identified sources within the RoI included in each fit. The solar flare source is then identified at local maximum of the TS map. The 68% containment radius (or 1 σ statistical localization error) on the position corresponds to a drop in the TS value of 2.30 (4.61 and 9.21 correspond to 2 and 3 σ respectively). See Figure 3 for an example TS map of FLSF 2017-09-10.

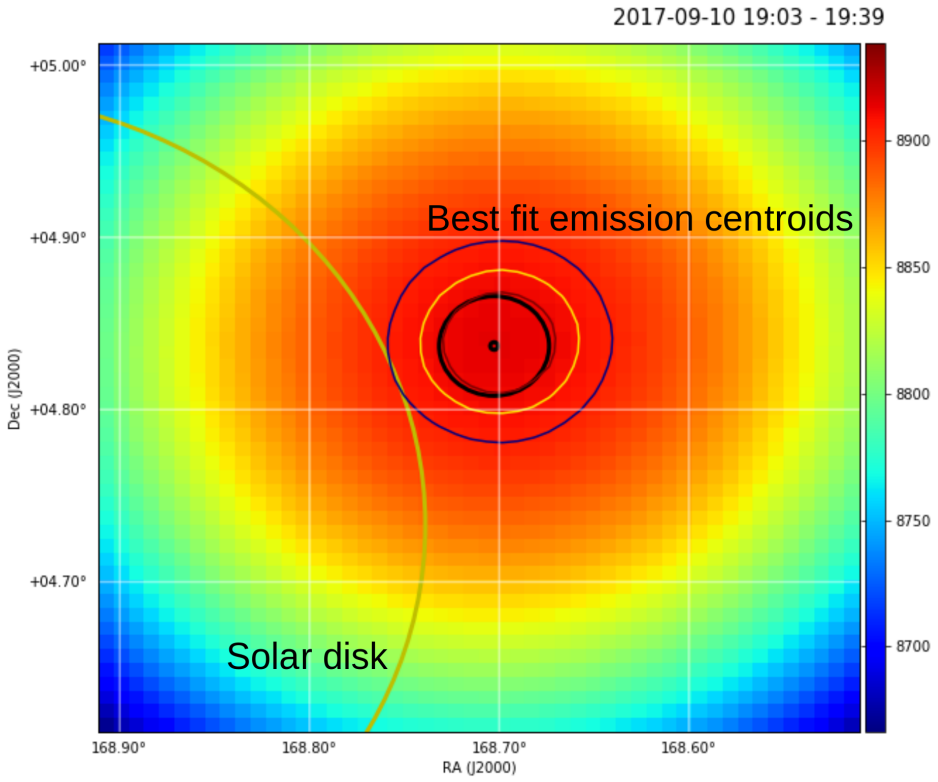

Fig. 3.— TS map for the observation of FLSF 2017-09-10 in the time interval of 19:03–19:39 UT. The large yellow circle represents the solar disk, solid black circle represents the 68% statistical error. The thin red, yellow and blue lines track the 1, 2 and 3 sigma contours on the TS map. These are not always perfectly circular, but a circular error containment region (black circle) provides a good approximation.

When performing the localization of the *Fermi*-LAT data of the Sun it is necessary

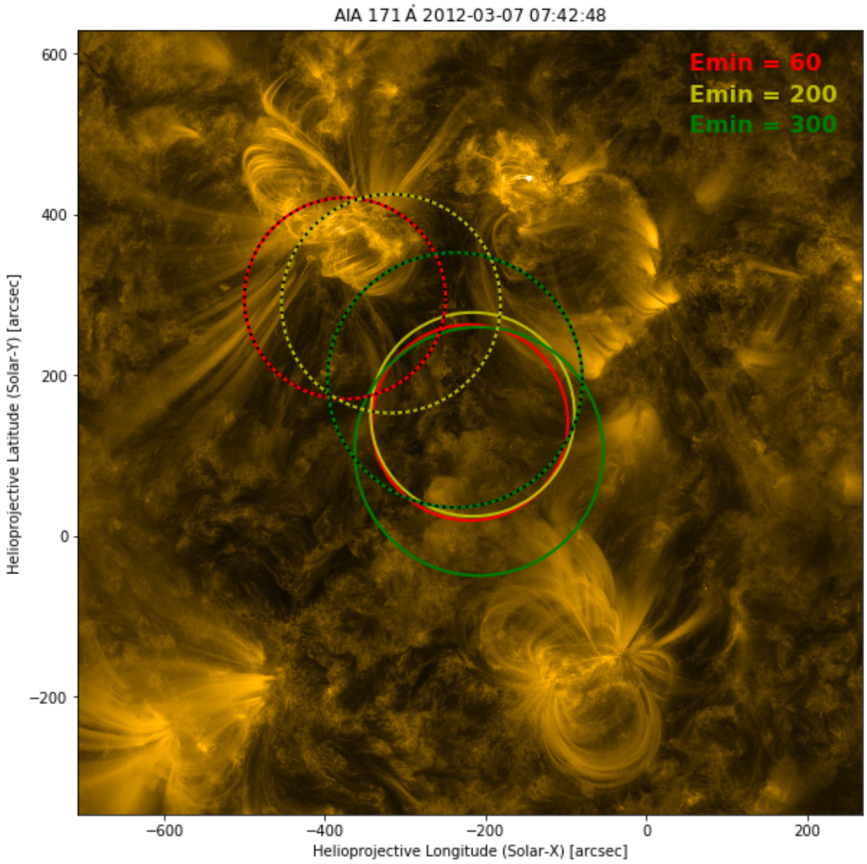

Fig. 4.— Comparison of the localization of the bright FLSF 2012-03-07 between fish-eye corrected (solid line) and not corrected (dashed line) with 60 (red), 200 (yellow) and 300 (green) MeV energy thresholds. Each circle marks the 68% statistical containment radius. The background is an Atmospheric Imaging Assembly (AIA) 171 Å image taken at 2012-03-07 07:42:48 UT by the Solar Dynamics Observatory (SDO)

.

to also take into account for the *fish-eye* effect. The fish-eye effect is a selection bias in the LAT trigger and reconstruction algorithms. At low energies and high incidence angles, particles that scatter toward the LAT boresight (having a smaller apparent incidence angle) are reconstructed with higher efficiency than particles that scatter away from the LAT boresight (having a larger apparent incidence angle). The reconstructed position of the source is biased and ends up appearing closer to the boresight axis than its true position.

The fish-eye effect can be quantified on an event-by-event basis using Monte-Carlo simulations. The correction depends both on the true incidence angle and the energy of the particle. The correction becomes dramatic at energies below 100 MeV and incidence angle greater than 70°, reaching several degrees shift (see Ackermann et al. 2012b, for a detailed description of the fish-eye effect).

The correction of the fish-eye effect is crucial particularly for bright flares, when the statistical error on the position becomes smaller than $0\overset{\circ}{.}1$ and the uncertainty becomes dominated by systematics. We investigated the effect of the fish-eye correction on two bright solar flares (FLSF 2012-03-07 and FLSF 2017-09-10). We varied the value of the minimum energy threshold to quantify the amplitude of the correction and the systematic error it induces. The amplitude of the fish-eye correction decreases with energy so we expect the distance between the corrected and uncorrected positions to decrease with energy. This is indeed what we observe in Figure 4: the correction is largest above a 60 MeV minimum energy, and above 300 MeV the two positions are consistent.

Solar flares generally have soft γ-ray spectra, cutting off at energies just above 100 MeV, so that the localization error (statistical) does not really improve as the threshold energy is increased, as can be seen in an example in Figure 4, where the statistical error on the localization above 300 MeV (green) is larger than the one above 60 MeV (red). Due to this, we use only photons with measured energies above 100 MeV when performing the localization study. Note that, although the localization uncertainties at 60 MeV and 100 MeV are very similar, the fish-eye correction that we had to apply to the events between 60 MeV and 100 MeV is larger than the one for the events above 100 MeV; therefore in order to minimize the systematic uncertainty, we use only events with energy >100 MeV to estimate the localization of the emission.

2.4.1. Localization of BTL FLSF 2014-09-01

The emission centroid for the other FLSFs previously published all remained within the 68% error radius with the new analysis tool, the FLSF 2014-09-01 is the only exception that we found during the analysis performed for this work.

As mentioned in section 2.4 the tool used to perform localization studies for the FLSF catalog to compensate for the potential systematic errors tied to inhomogeneous exposures across the FoV for short detections is `gttsmap` and no longer the `gtfindsrc` tool. We also reported (in section 2.4) the study performed to quantify the impact on the localization results due to the fish-eye effect and showed that it depends on the energy and incidence angle of the source. For this reason, in the FLSF catalog we have decided to perform localization studies using `gttsmap` on bright flares with exposure times longer than 20 minutes, with incidence angles smaller than 60° and with energies greater than 100 MeV in order to avoid potentially large systematic effects in the resulting emission centroids.

The first detection window of the BTL FLSF 2014-09-01 unfortunately occurred when the Sun was at an angle of 67° from the LAT boresight and lasted for only 16 minutes and the emission centroid published in Ackermann et al. (2017) was obtained using the `gtfindsrc` tool. After a careful re-analysis of this flare with the new localization tool and the knowledge obtained from the fish-eye systematic study we find that the emission centroid for FLSF 2014-09-01 has moved with respect to the previously published value as can be seen in Figure 5.

2.5. Test for spatial extension

We test the possibility to measure spatial extension in the localization results of the bright FLSF 2012-03-07 and FLSF 2017-09-10 by using `fermipy` (Wood et al. 2017). This tool has been used in several *Fermi*-LAT publications (Di Mauro et al. 2018; Abeysekara et al. 2018; Ackermann et al. 2018; Ahnen et al. 2019). It is based on a binned likelihood

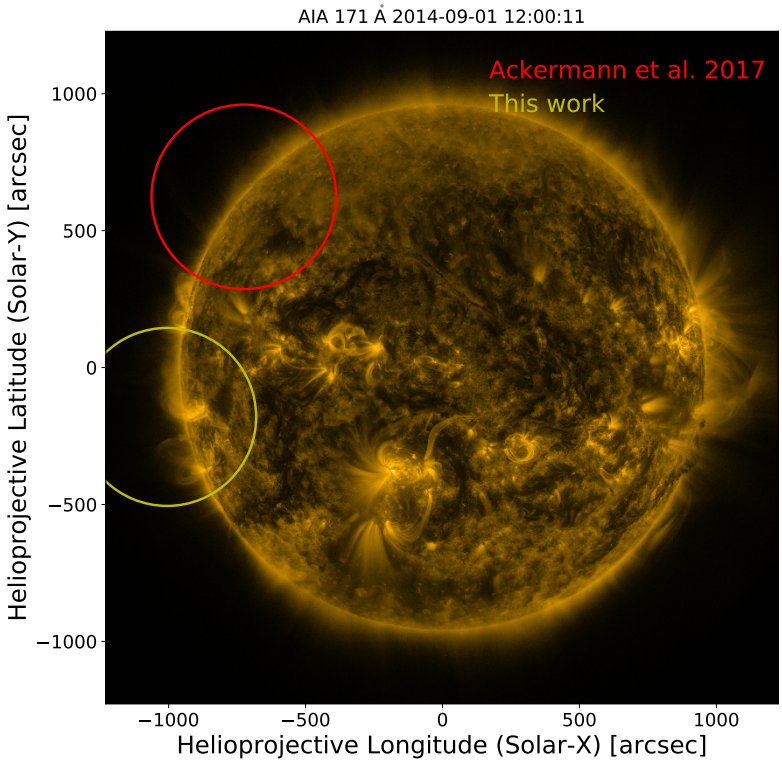

Fig. 5.— Emission centroid for FLSF 2014-09-01 for energies greater than 100 MeV with 95% uncertainty error radius using the `gttsmap` tool and the fish-eye correction in yellow and the previously published position is shown in red (with the 95% uncertainty error radius). The new position is centered at helioprojective coordinates X,Y=[-1105″,-128″] with a 95% uncertainty error radius of 643″.

analysis and, although not optimal for low counting statistics[12], presents the advantage of being very fast and allows to study the extension of γ-ray emission by comparing a model with a source with a radial extension (uniform disk or gaussian) with the data, and profiling the value of the $\log(\mathcal{L})$ by varying the extension radius.

For FLSF 2012-03-07 we use the same time window used in (Ajello et al. 2014),

[12]Both FLSF 2012-03-07 and FLSF 2017-09-10 are very bright and a binned likelihood analysis is appropriate.

namely from 2012-03-07 02:27:00 UT to 2012-03-07 10:14:32 UT, thus avoiding the time interval affected by ACD pile up. For FLSF 2017-09-10 we use the time window from 2017-09-10 15:56:55 UT to 2017-09-11 02:00:21 UT and SOURCE class events with energies greater than 100 MeV. The RoI is 10° wide. In this analysis the spectra of the FLSFs are described by a power law with exponential cut off, and the model is re-optimized during the fit procedure. For convenience, we use `ThreeML` (Vianello et al. 2015) as an interface to `fermipy`. It allows us to perform the fit to the LAT data using the `fermipy` plugin, providing, at the same time, an easy interface to download the data and build the model to be fitted. In Figure 6 we show the radial profile of a point source model compared to the data, for the best fit model. The model (which is convolved with the IRFs of the instrument), matches very well the radial profile of the counts in both directions, and no residual counts that could suggest the presence of a spatially extended emission are visible. Note that in our analysis we first optimize the localization of the source (hence the offset in Figure 6) and then we test for an extension. The optimized locations are at helioprojective coordinates X,Y=[-400″,400″] with a 68% uncertainty error radius of 100″ for FLSF 2012-03-07, and X,Y=[600″,-60″] with an uncertainty of 70″ for FLSF 2017-09-10.

Finally, in Figure 7 we show the profile of the likelihood as a function of the radial extension for two different spatial templates, for the two flares. The improvement with respect to the point source hypothesis is very small (ΔTS<1.5 in both cases), and only an upper limit of the radius can be placed. The 95% confidence level upper limits (corresponding to a $-\Delta \log(\mathcal{L}) \approx 1.35$) are, 0.°18, for the gaussian disk and 0.°14 for the radial disk for FLSF 2012-03-07, and 0.°23 (gaussian) and 0.°17 (radial) for FLSF 2017-09-10. These two events are the only two flares detected by the LAT that are bright enough to allow a dedicated spatial extension analysis. Even so, we can only set an upper limit on the extension that is smaller than the solar radius.

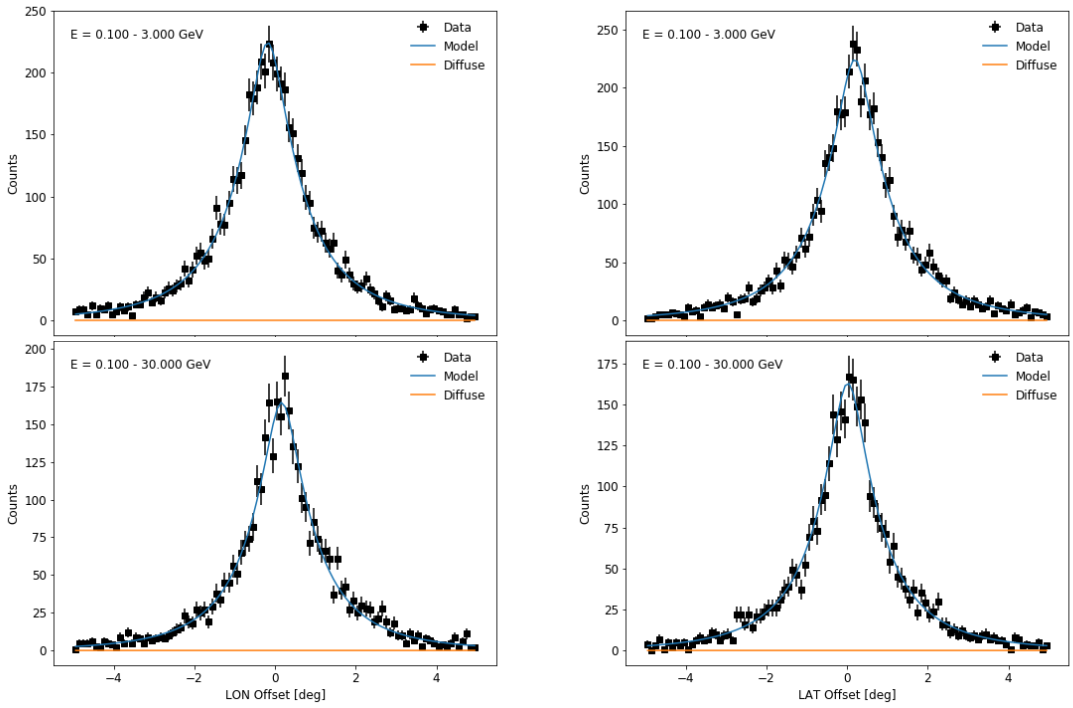

Fig. 6.— Longitude (left) and latitude (right) radial profile for FLSF 2012-03-07 (top row) and for FLSF 2017-09-10 (bottom row). The x-axis shows the offset with respect to the optimized localization.

2.6. Total emission duration, fluence and total number of greater than 500 MeV protons

With the Sun being observable by the LAT for only 20 to 40 minutes every 1.5 to 3 hours, it can be challenging to reconstruct the complete light curve and to estimate the true duration of the γ-ray emission. In order to overcome the issues caused by the observational gaps, we are forced to make some assumptions on the behavior of the emission when the Sun is outside of the FoV of the LAT. To identify the start of the FLSF we rely on the timing of the associated GOES X-ray flare. For example, when the GOES X-ray flare occurs during a LAT data gap and the start of the LAT detection window ($t_{\rm start}$) occurs after the end of the GOES X-ray flare we take the end of the GOES X-ray flare as the start of the γ-ray emission. For the cases where the GOES X-ray flare occurs within the

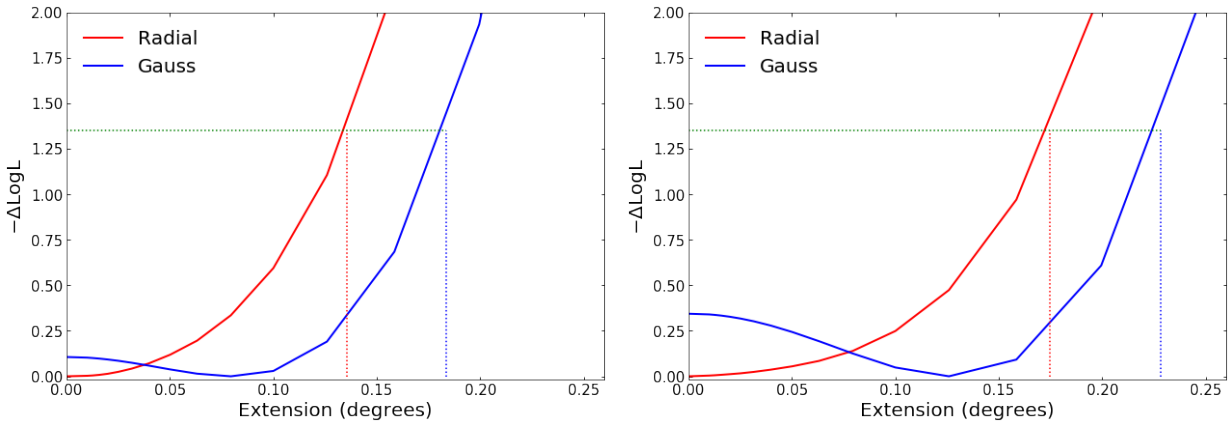

Fig. 7.— Likelihood profile of FLSF 2012-03-07 (left) and FLSF 2017-09-10 (right) as a function of a spatial profile for a Gaussian profile (Gauss) and a Radial profile (Radial). The horizontal green dotted lines show the increment of the $-\Delta \log(\mathcal{L}) \approx 1.35$, corresponding to a C.L. of 95%. The blue and red dotted lines are the estimated values for the upper limits on the radius.

detection window, and the LAT statistics are not sufficient to perform a fine time binning analysis, we take $t_{\rm start}$ to be the start of the detection window. The end time of the FLSF ($t_{\rm stop}$) is taken as the midpoint between the end of the last detection window and the start of the following observational window (with an upper limit on the γ-ray emission from the Sun). The total duration of the FLSF is then simply $\Delta t = t_{\rm stop} - t_{\rm start}$. These assumptions on the start and stop of the FLSF are not needed for the short prompt FLSF flares where the true start/stop of the γ-ray emission can be identified within the observational window.

Once we have estimated the start and stop of the FLSF, we can build a functional shape[13] to describe the lightcurve of the FLSF even in the cases where we only have one detection point (see Figure 8). Having a full description of the lightcurve of the FLSF emission it is possible to evaluate the total γ-ray fluence by simply integrating the lightcurve over the estimated duration of the flare. When integrating we assume that the flux values at the start and end of the FLSF are equal to 4.6×10^{-7} ph cm^{-2}s^{-1} which corresponds to

[13]We use `scipy` splines to build the functional shape of the γ-ray lightcurve.

the >100 MeV quiet Sun emission.

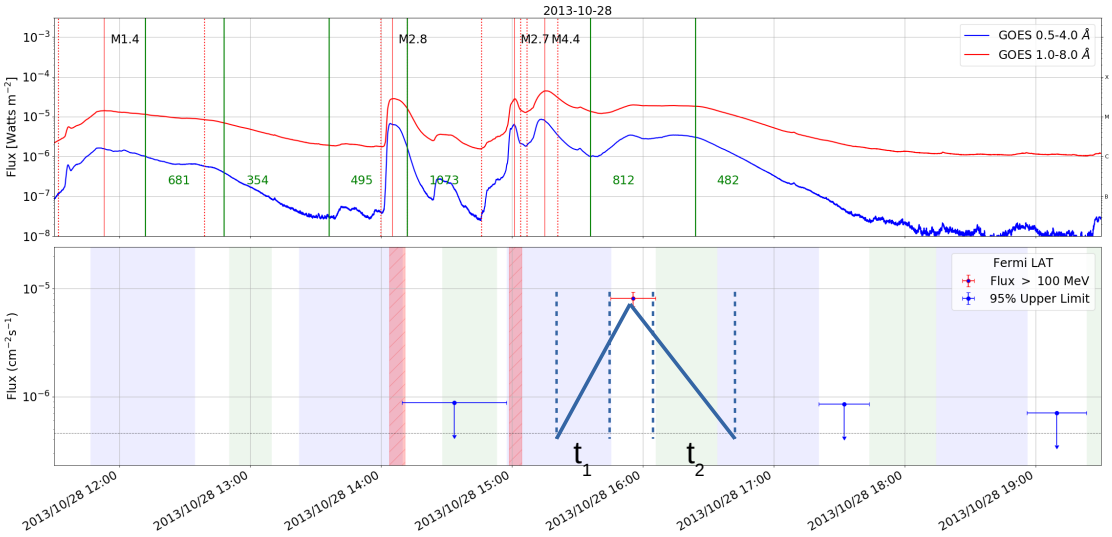

Fig. 8.— Lightcurve of the >100 MeV emission from FLSF 2013-10-28 with multiple flaring episodes prior to the start of the γ rays. The M2.7 and M4.4 and 812 km s^{-1} CME all from the same Active Region (AR) are likely associated with the γ-ray emission, although it is possible that the activity from another AR (M2.8 flare and 1073 km s^{-1} CME) may contribute to the γ-rays. The solid green lines represent the Large Angle and Spectrometric Coronagraph (LASCO) CME C2 first appearance, the linear speed value is annotated next to the line (also in green). The dashed/solid red lines represent the start(stop)/peak of the GOES X-ray flare, the GOES class is also annotated next to the solid red line. In the lower panel the vertical dashed lines denote the t_1 and t_2 quantities, where t_1 is defined as the time between the assumed start of the emission and the start of the detection window and t_2 is the time between the end of the detection window and the assumed end of the emission. For further details on how we use the t_1 and t_2 quantities to determine the uncertainties on the total fluence and total N500 see text in Section 2.6. The solid triangle represents the assumed lightcurve for this flare. The light green bands indicate when the *Fermi* satellite was in the South Atlantic Anomaly (SAA), the blue bands indicate when the Sun was outside of the FoV of the LAT and the pink bands indicate the presence of potential pile-up in the data.

For every FLSF that is best described by the pion template model we provide an estimate of N500 needed to produce the γ-ray emission detected in the observational time window. However, if we want to know the total N500 needed to produce the total γ-ray emission over the full duration then we need to build a functional form (just as was done for the lightcurve) also for the temporal evolution of N500. The start and stop of the FLSF remain the same as described above; the main challenge lies in estimating the value for N500 at t_{start} and t_{stop}. The value of N500 depends on two parameters, the normalization of the spectral function used to fit the data and the best proton index resulting from the spectral analysis (as described in 2.3). We therefore find the best value for the N500 corresponding to the quiet Sun flux level by performing a scan over all the possible proton indices (ranging from 2 to 6 with the same gradation as used during the likelihood analysis) and used the average value of 6×10^{22}. Finally, as in the case for the fluence, we integrate the functional form to find N500 needed to produce the total emission of the FLSF. The values for the total fluence and total N500 with their associated uncertainties for all the FLSFs in the catalog are listed in Table 1.

The main uncertainties on the fluence and total N500 are due to the values of t_1 and t_2, where t_1 is defined as the duration between the assumed start of the emission (t_{start}) and the start of the detection window and t_2 is the duration between the end of the detection window and the assumed end of the emission (t_{stop}). See Figure 8 for an illustration of t_1 and t_2 for the case of the single point detection of FLSF 2013-10-28. To estimate this uncertainty we vary the value of t_1 and t_2 by $\pm50\%$ and repeat the integral over the flux and N500, the error is then found by taking the difference between this value and the nominal one.

3. FLSF classification

We associate each significant detection of γ-ray emission from solar flares with solar events as seen by other instruments. For most cases the association of the γ-ray emission

to a specific GOES flare or CME is straightforward: linking the FLSF to a single flare or CME within an hour of the start of the γ-rays. In some cases however, the association to a single GOES flare or a single CME is not obvious when several events happen within a short time frame. In these cases, we tend to pick the GOES flare or the CME closest in time to the γ-ray emission. For example, the FLSF 2013-10-28 (shown in Figure 8) a series of three M-class flares occurred, accompanied by two CMEs, all prior to the γ-ray detection. In this case the γ-ray emission is likely associated with the pair of flares M2.7 and M4.4 (both of which started within an hour of the start of the FLSF) from the same AR and the associated CME with speed 812 $\mathrm{km\,s^{-1}}$ (LASCO first appearance occurred $\approx$15 minutes prior to the start of the FLSF).

In the cases of the BTL FLSFs, the soft X-ray emission detected by GOES is either absent or biased toward lower fluxes than would have been the case if it was a disk flare. For those, the STEREO satellites provide the direct Extreme Ultra Violet (EUV) observation of the flare, which allows us to estimate the peak soft X-ray flux (for a detailed description of this procedure, see Ackermann et al. 2017).

Once we have found a GOES X-ray flare associated with the FLSF then we can begin to classify the flares in the catalog. In the attempt to better characterize the features present in each of the FLSFs and hopefully to also understand the underlying acceleration mechanisms at work during the flares in the FLSF catalog, we compare the γ-ray timing evolution with that in Hard X-Rays. This is because HXR emission traces the high-energy electron population accelerated during the flare energy release and γ-ray signatures of protons accelerated by the same processes and on the same time-scales have been observed in the past by SMM and EGRET (Thompson et al. 1993).

The *Fermi*-Gamma-Ray Burst Monitor (GBM, Meegan et al. 2009) on-board the *Fermi* satellite consists of twelve NaI detectors and two BGO detectors covering an energy range 8 keV to 40 MeV. Thanks to the fact that the *Fermi*-GBM continuously monitors the non occulted sky, it provides excellent HXR coverage of the FLSFs in this catalog. For each FLSF in the catalog with a time window coincident with the prompt phase of an X-ray solar

flare, we compare the HXR evolution observed by the two instruments of the *Fermi*-GBM to a finely time-resolved γ-ray lightcurve as shown in Figure 9 for the FLSF 2011-09-06. If we find that the γ-ray emission evolution is synchronous to the HXR evolution we classify it as a *prompt* flare.

When performing these finely time-resolved lightcurves different patterns emerge revealing a more complex picture of the γ-ray solar flares. This can be seen again for the FLSF 2011-09-06 (Figure 9). A prompt component coincident with the bright HXR peak appears in γ-rays and is immediately followed by a second phase lasting for more than 20 minutes after the start of the flare. This phase consists of a second less bright peak with a longer rise and fall timescales, but there is no sign of such behavior in the HXRs. The Sun passed in the FoV two hours later and no γ-rays were detected. Cases such as the FLSF 2011-09-06 are classified as *prompt short-delayed*.

A flare is *prompt-only* if the γ-ray emission does not extend beyond the HXR duration, as was the case for the flare detected on 2010-06-12 (Ackermann et al. 2012a). All flares detected through the LLE method are associated with prompt emission, but some exhibit delayed emission as well. The fine time-resolved lightcurves for all the FLSFs classified as *prompt* are reported in Ajello et al. (2020).

A large number of solar flares observed by the *Fermi*-LAT do not fall in the *prompt* category: γ-ray emission is detected beyond the end of the HXR emission and even the end of the SXR seen by GOES. We refer to that general category as *delayed* emission. The subset of flares classified as *delayed* also exhibit a wide variety of behaviors. For example there are cases where no significant γ-rays are detected during the prompt phase of the flare in X-rays, but γ-ray emission seen rising and falling later on. We refer to these flares as being *delayed-only*.

One of the most interesting results of the *Fermi*-LAT observations of solar flares are the events with detectable emission lasting several hours. As already discussed in Section 1, the LAT has the Sun in its FoV on average only 40% of its orbit, greatly limiting the

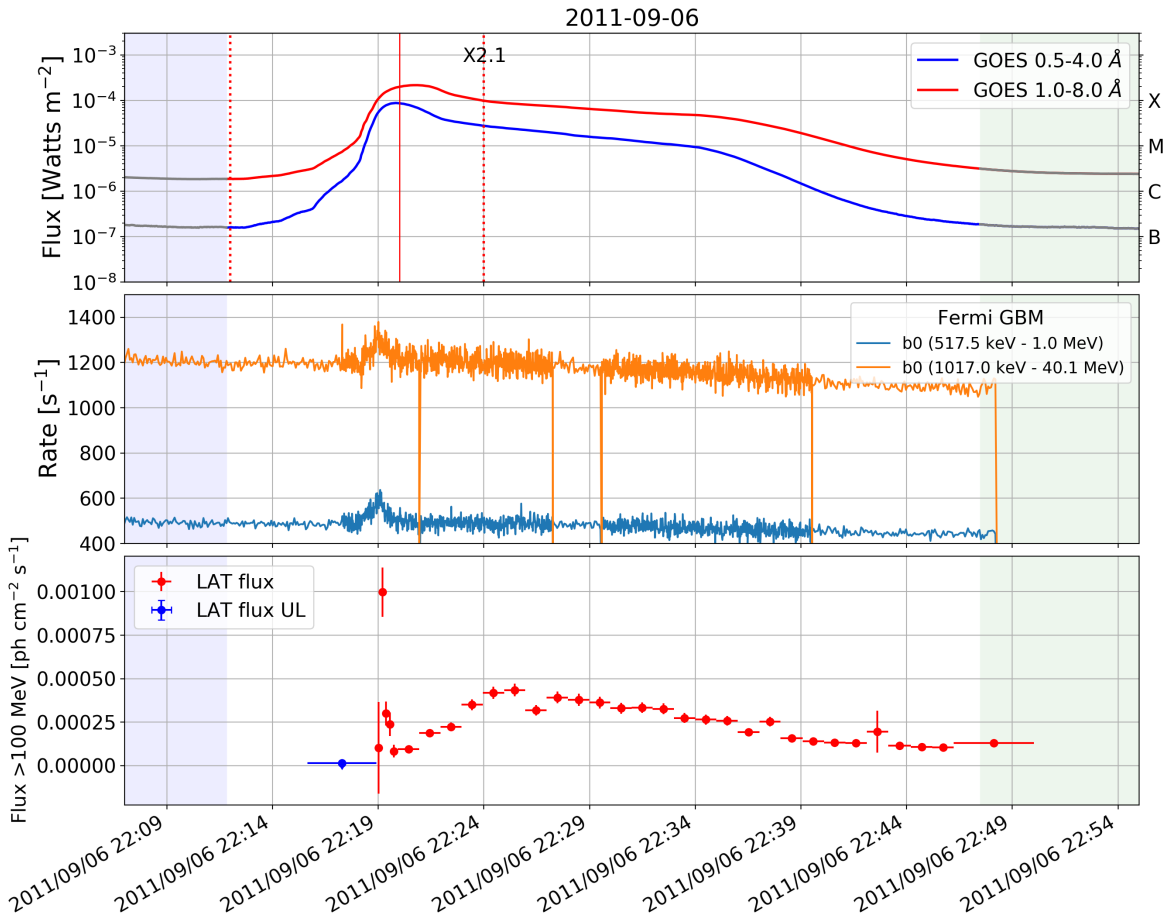

Fig. 9.— Example of a flare with a prompt component coincident with the bright HXR peak followed by a γ-ray delayed emission; that occurred on 2011-09-06. From top to bottom, the GOES X-ray flux in two energy bands, the *Fermi*-GBM X-ray lightcurve and the *Fermi*-LAT >100 MeV flux using the standard likelihood analysis with a fine time binning to reveal the *prompt* component. The dashed/solid red lines represent the start(stop)/peak of the GOES X-ray flare, the GOES class is also annotated next to the solid red line.

coverage of these *delayed* γ-ray flares. As a result it is difficult to study the time profiles of these flares throughout the entire duration of the emission.

This is the case of the FLSF 2012-03-09, which is associated with a GOES M6.3 flare with HXR extending up to the GBM NaI 100–300 KeV channel. Most of the prompt phase

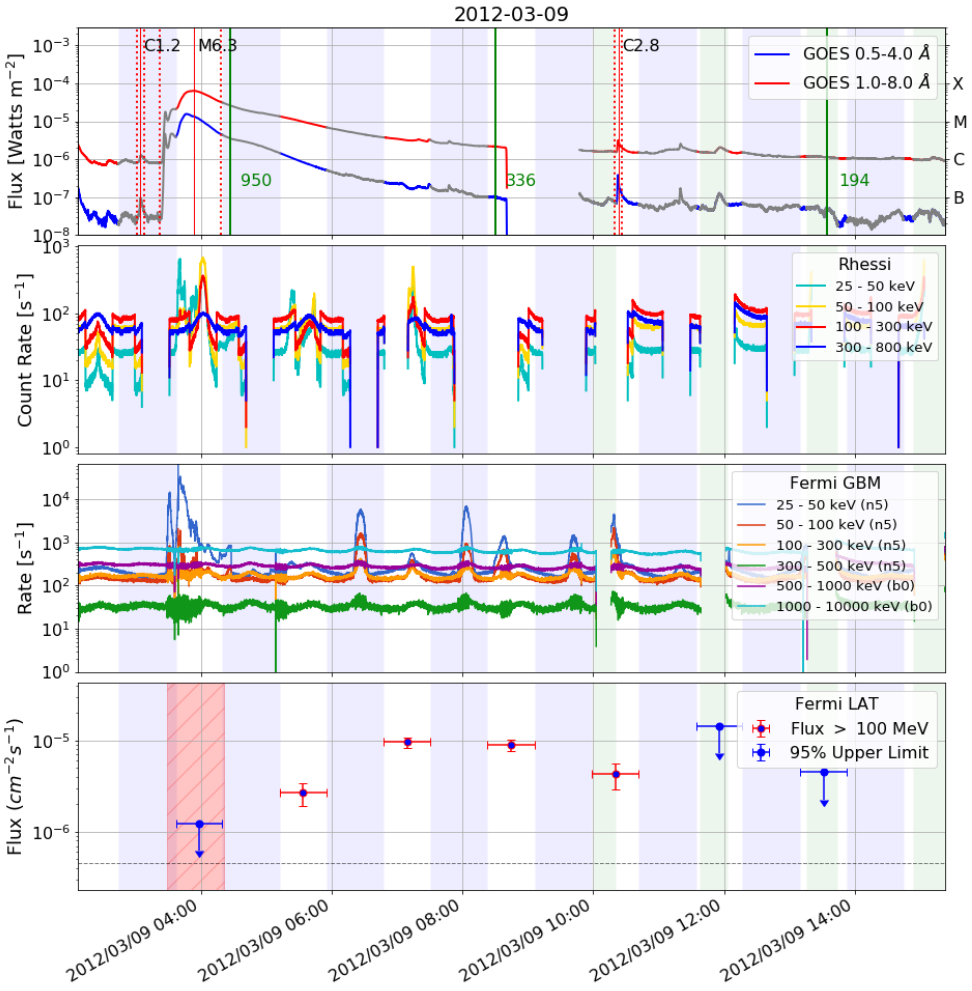

Fig. 10.— Lightcurve of the >100 MeV emission from FLSF 2012-03-09 lasting more than 6 hours but with no detectable high-energy γ-ray emission in the impulsive phase, classified as *delayed-only*. The four panels report the light curve measured by GOES, RHESSI, *Fermi*/GBM and *Fermi*/LAT in various energy ranges. The solid green lines represent the LASCO CME C2 first appearance, the linear speed value is annotated next to the line (also in green). The dashed/solid red lines represent the start(stop)/peak of the GOES X-ray flare, the GOES class is also annotated next to the solid red line. The light green bands indicate when the *Fermi* satellite was in the SAA and the blue bands indicate when the Sun was outside of the FoV of the LAT. Pink bands indicate the time interval over which potential pile-up effects could be present.

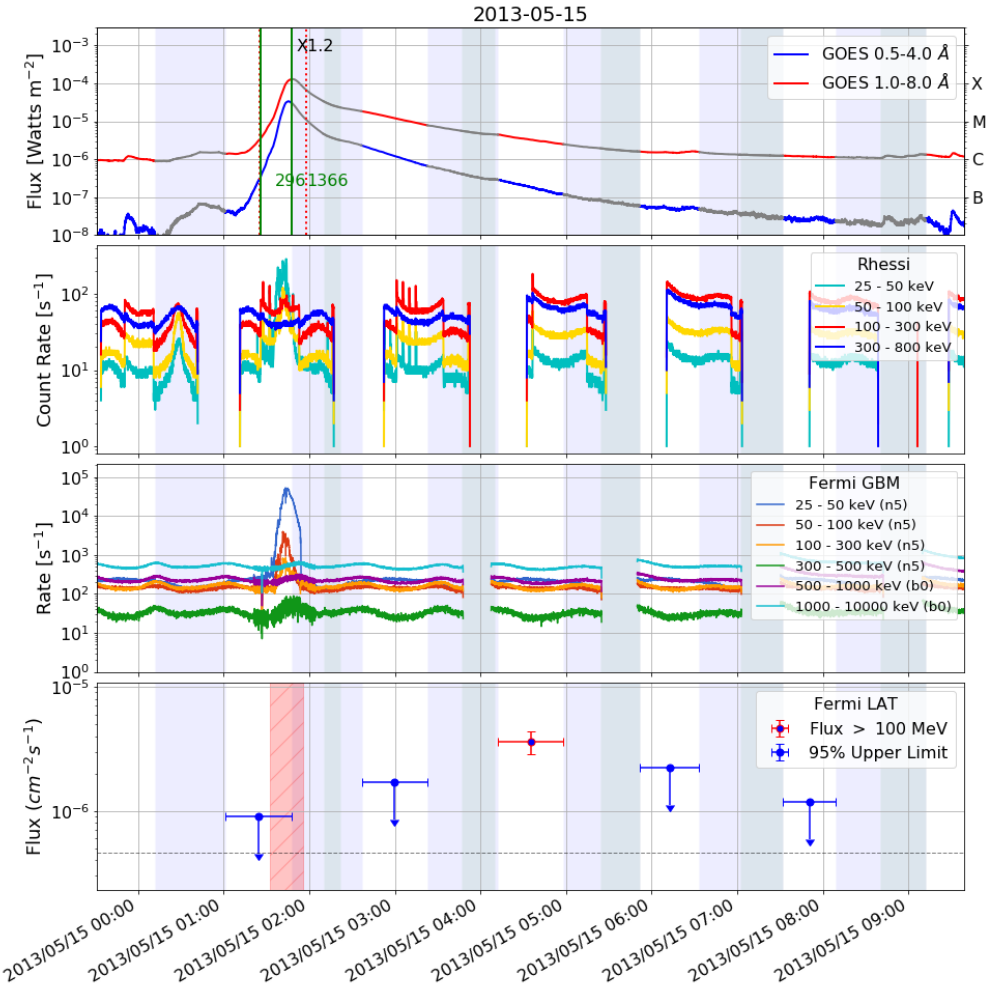

Fig. 11.— The *delayed-only* lightcurve of the >100 MeV emission from FLSF 2013-05-15 flare with no detectable high-energy γ-ray emission in the impulsive phase, or the following time window. The four panels report the same quantities as those in Figure 10.

was observable by the *Fermi*-LAT and the bright SXR affected the instrument response (bad time interval in red in Figure 10). No γ-ray emission was detected during the peak of the prompt phase using the S15 event class or the LLE analysis method. Yet γ-ray emission was detected when the Sun came back in the FoV, almost two hours after the start of the flare in X-rays, and lasted for four orbits. It followed a rise and fall pattern reaching its peak after four hours and ending 7 hours after the start of the flare in X-rays.

Similarly, the FLSF 2013-05-15 with no significant emission detected during either the

impulsive phase or in the first time window following the flare, but significant emission detected in the following time window (Figure 11). In itself, it might not be a new type of behavior, as it can be seen as a rise-and-fall pattern with the starting flux being just below the *Fermi*-LAT sensitivity but the peak flux being high enough to be detected.

These behaviors highlight the possibility that high-energy emission above 100 MeV can arise at later times, even if the prompt phase itself did not show a strong non-thermal component (almost no HXR above 300 keV and no γ-rays below 30 MeV). Although these cases are rare (only four cases in the catalog), they are particularly interesting in understanding whether the acceleration of high energy particles is solely due to the prompt phase of solar flares or due to a separate mechanism entirely.

There are also FLSFs with both a clear prompt and a long duration delayed component present, these flares are classified as *prompt-delayed*. An example of this class of flares is the FLSF 2017-09-10 (Omodei et al. 2018) that exhibited a very bright prompt phase and almost 14 hours of delayed γ-ray emission. In the FLSF catalog we were able to classify the flares into six different categories: *prompt*, *prompt-only*, *delayed*, *delayed-only*, *prompt short-delayed*, *prompt-delayed*. All the lightcurves and categories of the FLSFs are reported in Ajello et al. (2020).

4. Results

Continuous monitoring of the Sun has led to the high-confidence (TS$\geq$30) detection of 45 solar flares with γ-ray emission above 60 MeV. For 39 of these flares γ-ray emission was significant in 92 `SunMonitor` time windows. The remaining 6 flares were detected with LLE analysis only. Of these 45 flares, 6 are classified as *prompt-only*, 4 are classified as *delayed-only* and for 10 flares both the *prompt* and *delayed* emission was clearly observed by *Fermi*-LAT. For the remaining cases, we cannot exclude the presence of a *prompt* emission because the Sun was not in the FoV of the LAT during the HXR activity. Because of the observing strategy of the *Fermi*-LAT, more than half of the solar flares detected are only

detected in a single time window, whereas 16 are detected in more than one window. Of the 16 flares detected in multiple time windows 5 are detected in only 2 time windows, and 11 are detected in 3 or more (up to 11) time windows well beyond the HXR signatures of the high-energy electrons. Seven flares in the latter group show a well-defined pattern of rise and decay phases after the end of the HXR and 2 show a decay phase only. All 5 flares detected in 2 time windows show a decay between the two points. Some of these may represent a rise and fall case with a peak occurring in between the two time windows. However, this is unlikely because statistically one would expect 2 or 3 of these flares showing rise instead of decay, and because this would imply faster rise and fall than seen in the flares with more than three windows of observation.

In Table 1 we show the time integrated results for the FLSFs detected with the `SunMonitor`. The columns report the report the LAT detection start date and time, the GOES soft X-ray start and end times, the LAT detection duration, the total duration of the FLSF[14], the fluence, namely the time-integrated flux over the total duration, the FLSF flare type, and the total number of accelerated >500 MeV protons (N500). The GOES classes for the three BTL flares (identified by *) are estimated based on STEREO UV fluxes as described in Pesce-Rollins et al. (2015).

The characteristics of the γ-ray emission in each `SunMonitor` time window are listed in Table 2. Results from flares detected in more than one time window are listed together. The columns of Table 2 are the time of each detection window, the duration of the window, the >100 MeV flux, TS, and the spectral parameters (power-law indices and cutoff energies) of the best fitting photon model. For the cases where the ΔTS>9 we give the proton index based on pion-decay model in the last column. The fluxes are given in 10^{-5} ph cm^{-2}s^{-1} and calculated for the emission between 100 MeV and 10 GeV. The LAT emission in all `SunMonitor` time windows with TS larger than 70 shows significant spectral curvature and

[14]The detection duration is simply the sum of the `SunMonitor` detection windows duration while the total duration is that found using the approach described in section 2.6.

can be well described with the exponential cutoff model. This does not mean that all fainter γ-ray flares are only consistent with a power law model, but rather that the lower statistics make it impossible to distinguish between the two.[15]

We retract the LAT detection of the C-class flare on 2011-06-02 reported in Ackermann et al. (2014b), because during the month of June, the Sun passes through the galactic plane, and a higher background flux of photons enters into the RoI around the Sun relative to other periods in the year. After careful re-analysis of this event, we found that the reported detection was not statistically significant.

The FLSF LLE catalog results are reported in Table 3. Three of the flares detected with LLE were outside the nominal LAT FoV. For the eleven flares in the FoV, five were not detected above 60 MeV by the `SunMonitor` analysis, and an upper limit was obtained for the time window when the flare happened. For the six flares detected with both analyses in the same time window, the >100 MeV fluxes reported in the `SunMonitor` results (Table 1) are the average over the time window, and the >100 MeV fluxes obtained through the LLE approach are listed in Table 3.

The durations for the flares detected with the `SunMonitor` range from 0.6 to 20.3 hours, whereas the LLE detected flares have durations ranging from 10 to 400 seconds (see Figure 12). Both the >100 MeV peak γ-ray fluxes and total number of >500 MeV protons needed to produce the observed γ-ray emission for all of the FLSFs in the catalog span over four orders of magnitude (see Figure 13).

Eight of the 45 FLSFs have durations of two hours or more. Their >100 MeV fluxes as a function of time (since the start of the associated GOES X-ray flare) are shown in Figure 14. The time profiles of all these *delayed* FLSFs follow a rise-and-fall behavior. However, the rise times to reach the peak flux and the fall times vary significantly from flare to flare. For example, the FLSF 2017-09-10 has a rise time of $\approx$1.5 hours while the

[15]The FLSF of 2013-10-28 is the only exception, having a TS of 120 and the exponential cutoff model is not preferred (ΔTS=8).

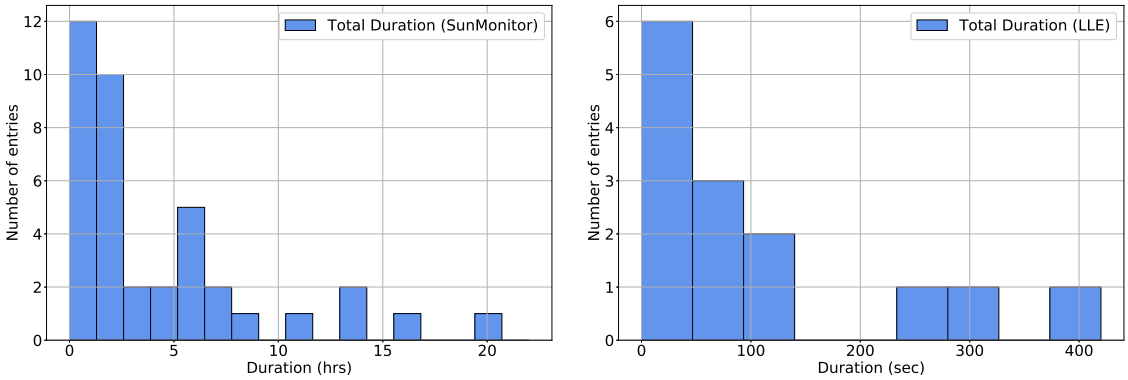

Fig. 12.— Distribution of the total duration for all of the `SunMonitor` detected flares (in hours, left panel) and the LLE detected flares (in seconds, right panel) in the FLSF catalog.

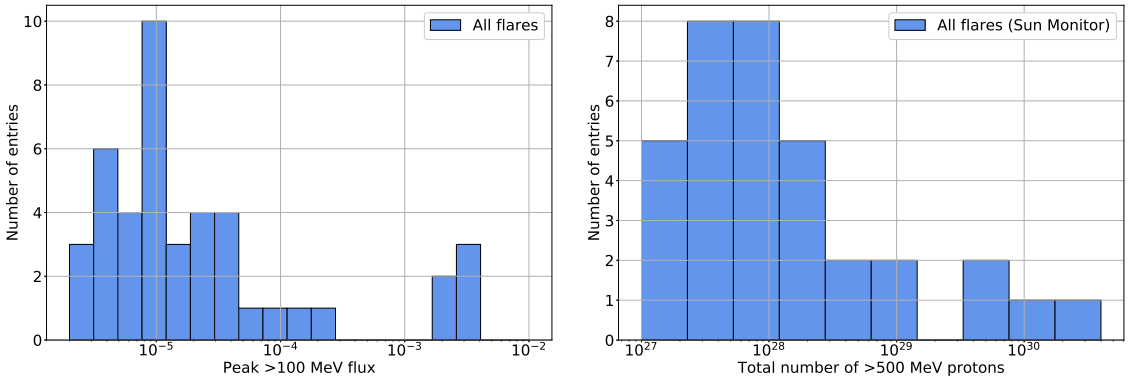

Fig. 13.— Distributions of the peak >100 MeV flux (in ph cm^{-2} s^{-1}; left panel) for all FLSFs in the catalog, and the total number of accelerated >500 MeV protons needed to produce the detected γ-ray emission for each of the `SunMonitor` detected FLSFs (right panel).

FLSF 2017-09-06 takes ≈4.5 hours to reach its peak. The peak flux values also vary from flare to flare by up to two orders of magnitude, emphasizing the wide variety of these *delayed* flares. The two brightest flares in Figure 14 were coincident with very strong SEP events; Ground Level Enhancement (GLE)#72 in the case of the FLSF 2017-09-10 and

a sub-GLE event in the case of the FLSF 2012-03-07[16]. Coincidentally, the γ-ray fluxes for these two flares are more than an order of magnitude higher than the other events. In Table 4 we list some multiwavelength associations with the FLSFs presented in this work. In particular, we include GOES X-ray flares, CMEs, SEPs and Hard X-ray counterparts to the gamma-ray flares.

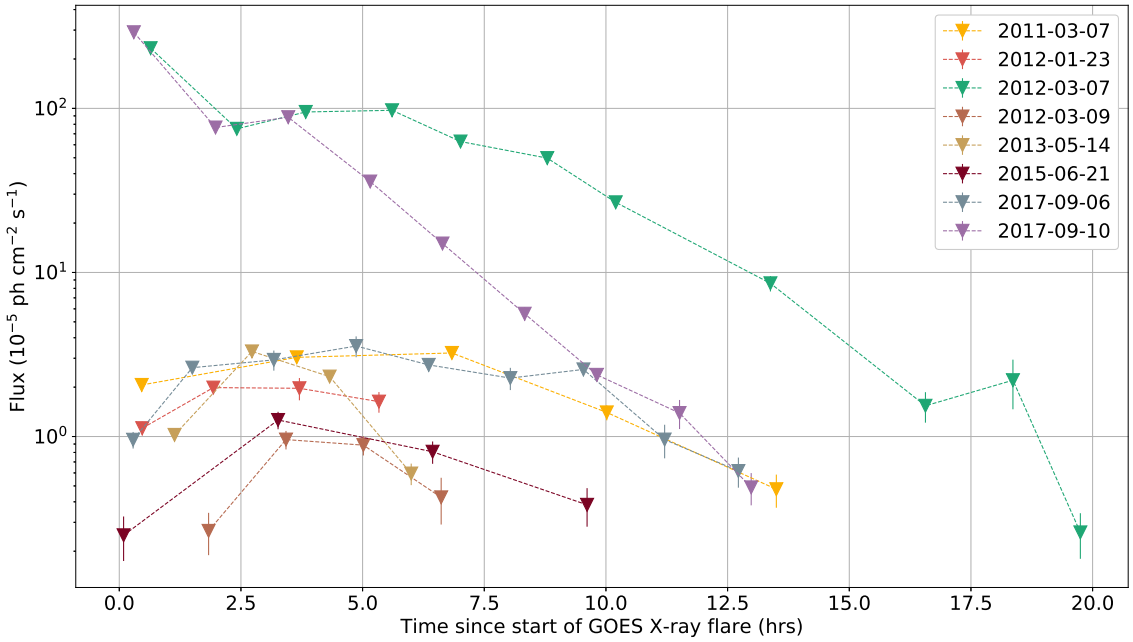

Fig. 14.— The time profiles of flux between 0.1 - 10 GeV for for each FLSF lasting two or more hours versus the time since the start of the GOES X-ray flare. The typical rise and fall behavior of the γ-ray emission during the *delayed* phase is most evident for the cases where no *prompt* emission was present during the detection.

For the FLSFs with more than 4 `SunMonitor` detection windows, it is possible to study the variation of the proton index with time. In Figure 15 we show the accelerated proton spectral index as a function of time since the start of the GOES X-ray flare (assuming that

[16]GLEs are sudden increases in the cosmic ray intensity recorded by ground based detectors. The number following the GLE indicates the number of GLEs that have been observed since 1956, see GLE database `http://gle.oulu.fi` for more details.

the γ-rays emission is due to pion decay). The statistical uncertainties limit the amount of information available from the time variation of the proton indices. However, the data suggest that the proton spectra tend to gradually steepen (get softer), following a trend similar to the γ-ray fluxes for these delayed flares.

For the extremely bright FLSF 2017-09-10, both the prompt and delayed phases were well observed by the LAT, and we are not limited by statistics. The data from this flare show three phases in the evolution of the proton index over the almost two hours of γ-ray emission (see Figure 16). This flare was also associated with GLE #72. and Kocharov et al. (2020) show that these phases correspond to separate components of the GLE.

Solar cycle 24 has been particularly poor in GLE events. Only two have been firmly identified: GLE #71 and #72, which occurred on 2012-05-17 and 2017-09-10. Both events were detected with the *Fermi*-LAT. In addition to GLEs, five "sub-GLE" events have been identified. Sub-GLE events are those detected only by high-elevation neutron monitors and correspond to less energetic events, extending to a few hundred MeV (Poluianov et al. 2017). They occurred on 2012-01-27, 2012-03-07, 2014-01-06, 2015-06-07, 2015-10-29 at levels of relative increase in neutron flux of 5%, 5%, 4%, 8% and 7%, respectively (smaller than the relative increase of 17% for GLE#71). The first three correspond to flares in the FLSF catalog, but no emission was detected for the last two.

Flares with both the LLE-prompt and delayed phases detected by the LAT allow a comparison of the prompt and delayed emission characteristics within the same flare. Seven flares in the catalog (2011-09-06, 2011-09-24, 2012-06-03, 2012-10-23, 2014-02-25, 2014-06-10 and 2017-09-10) satisfy this criterion. For these flares we found the peak flux value for the prompt phase by fitting the LLE data at the peak of the lightcurve with two models: a simple power-law or a power-law with an exponential cutoff using the `xspec` analysis package[17]. The correlation between the peak fluxes of the prompt and delayed phases are shown in the top panel of Figure 17 illustrating that, on average, the prompt

[17] `xspec` model `pegpwrlw` and `pegpwrlw*highecut`

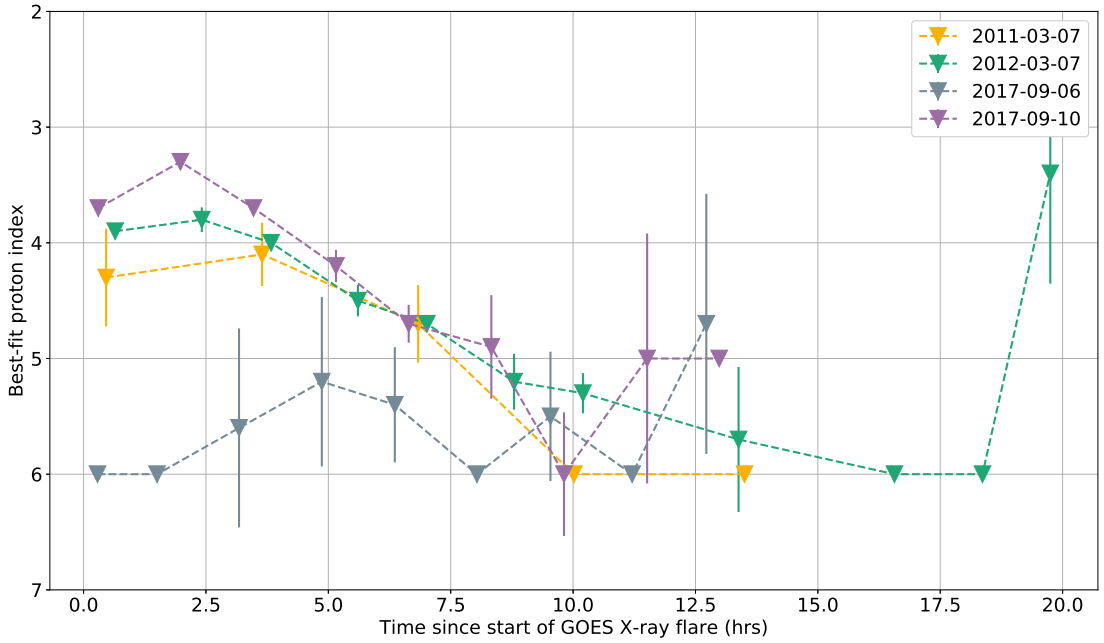

Fig. 15.— Variation with time (since start of the GOES X-ray flare) of best-fit proton spectral index for the four FLSFs for which a statistically meaningful measurement can be made.

peak flux is up to 10 times higher than the peak of the delayed emission. The bottom panel of this figure shows the correlation between the total γ-ray energies (> 100 MeV), showing a larger dispersion and a total energy released during the delayed phase that, on average about 10 times larger than that in the prompt phase.

The FLSFs in the catalog are almost evenly distributed between GOES M and X-class flares (in the 0.5 to 10 keV energy range), with 25 flare associated with X-class and 20 associated with M-class (see top panel of Figure 18, where the gray distribution represents all of the M and X-class GOES flares that occurred during the time period considered in this paper). As can be seen in the bottom panel of Figure 18, the FLSFs of *delayed* type are evenly distributed between the M and X-class flares while the *prompt* type flares are mostly associated with M GOES class flares (75% of the flares are M class). These distributions also illustrate how the increase in sensitivity of the LAT with respect the

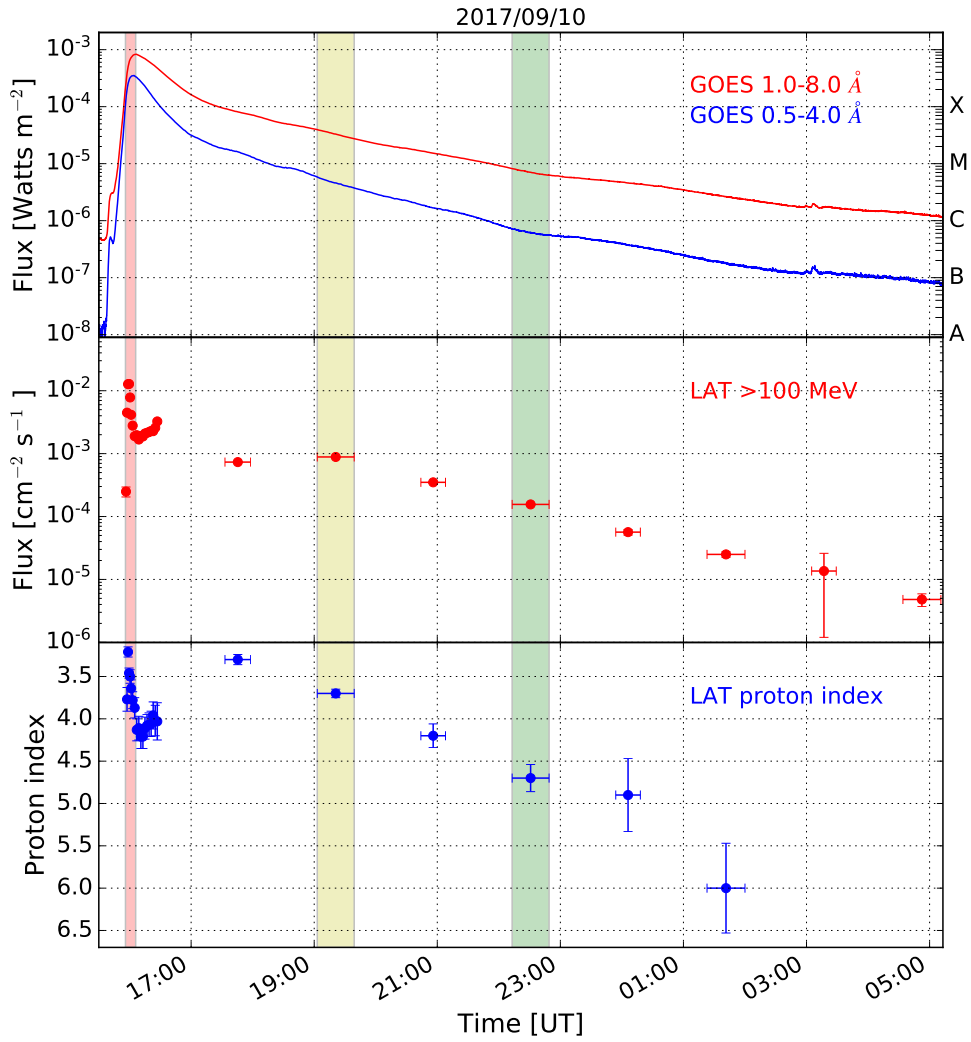

Fig. 16.— Composite light curve for the FLSF 2017-09-10 with data from GOES X-rays, *Fermi*-LAT >100 MeV flux and the best proton index inferred from the LAT γ-ray data. The figure is taken from Omodei et al. (2018). The evolution of the proton index shows three distinct phases, a softening during the prompt-impulsive phase, a plateau and another softening during the decay phase. The three color bands represent the time windows over which we performed the localization of the emission.

previous γ-ray detectors has allowed to detect >100 MeV emission over a wider range of GOES X-ray flares. Furthermore, when combining the information from Figures 18 and 19 it appears that the presence of a fast CME is more relevant for the *delayed* type flares than

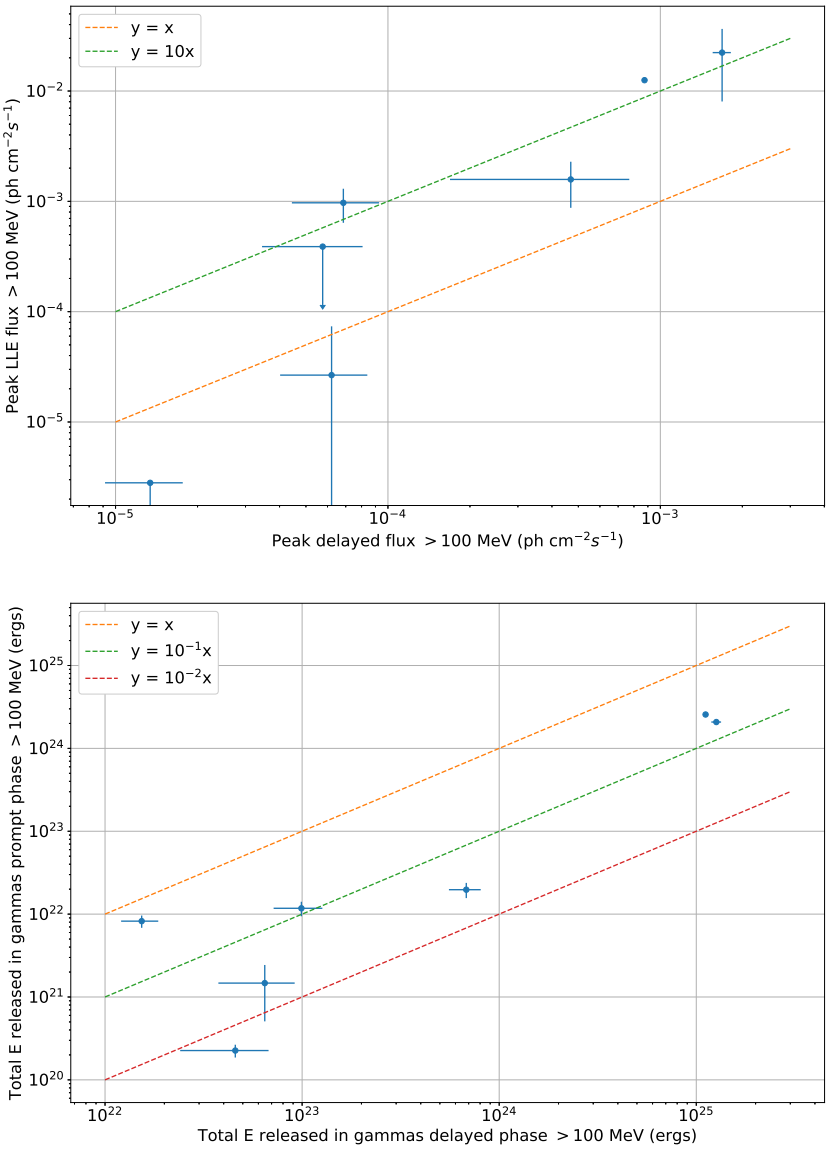

Fig. 17.— Scatter plot of the peak flux during the prompt phase versus the peak flux during the delayed phase for the 7 FLSFs with both the prompt a delayed phases observed fully. The prompt peak fluxes tend to be higher than those during the delayed phase, in some cases up to more than 10 times. Bottom panel: Scatter plot of the total energy released in γ-rays above 100 MeV during the prompt and delayed phases. The total energy released during the delayed phase is on average about 10 times larger than the prompt phase.

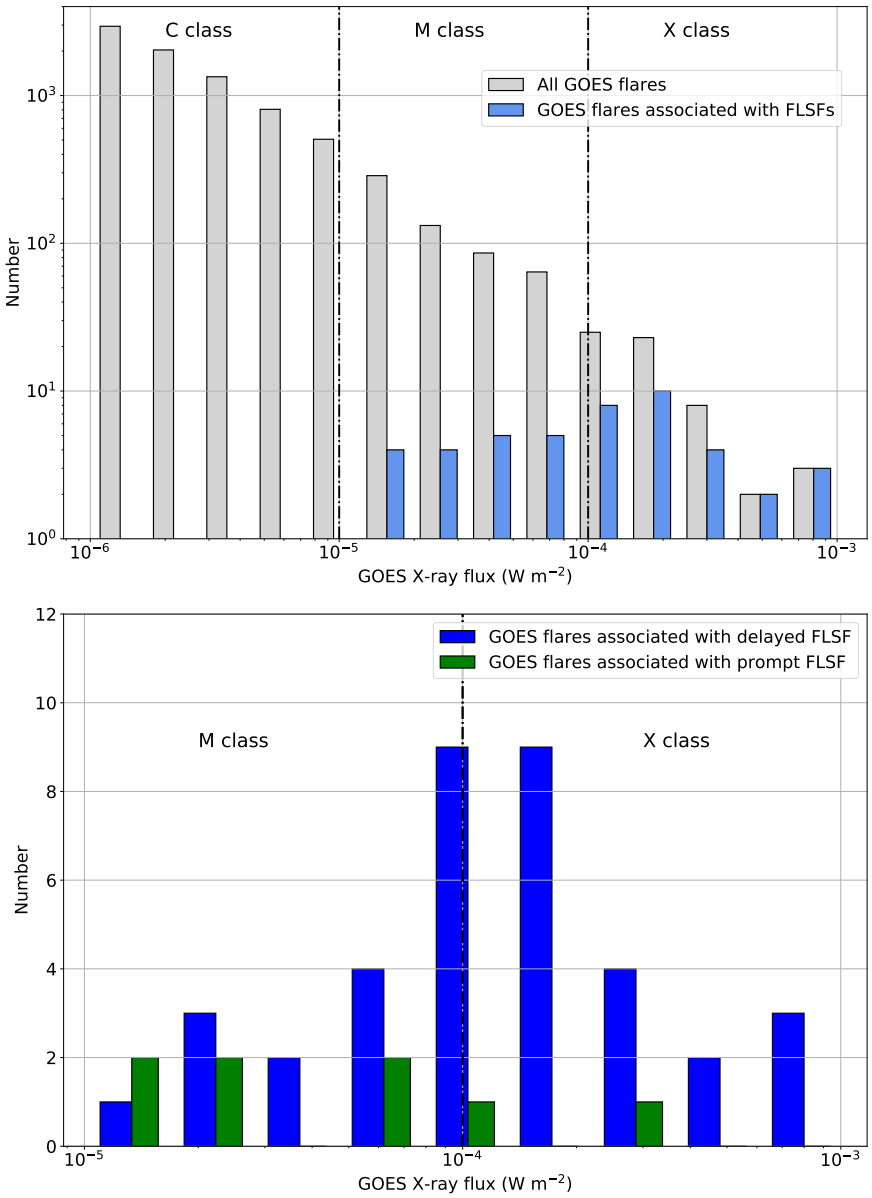

Fig. 18.— Top panel: Distribution of the GOES class for all of the X-ray flares of solar cycle 24 (in gray) and for the FLSFs (light blue). Bottom panel: Distribution of the GOES class for the FLSFs separated by type *delayed* (blue) and *prompt* flares (green).

the brightness of the associated X-ray flare.

During Cycle 24, the number of GOES M-class and X-class flares in the period covered by this catalog (January 2010 - January, 2018) was approximately the same in the first half as in the second (384 and 389, respectively), while the majority of fast CME events (those

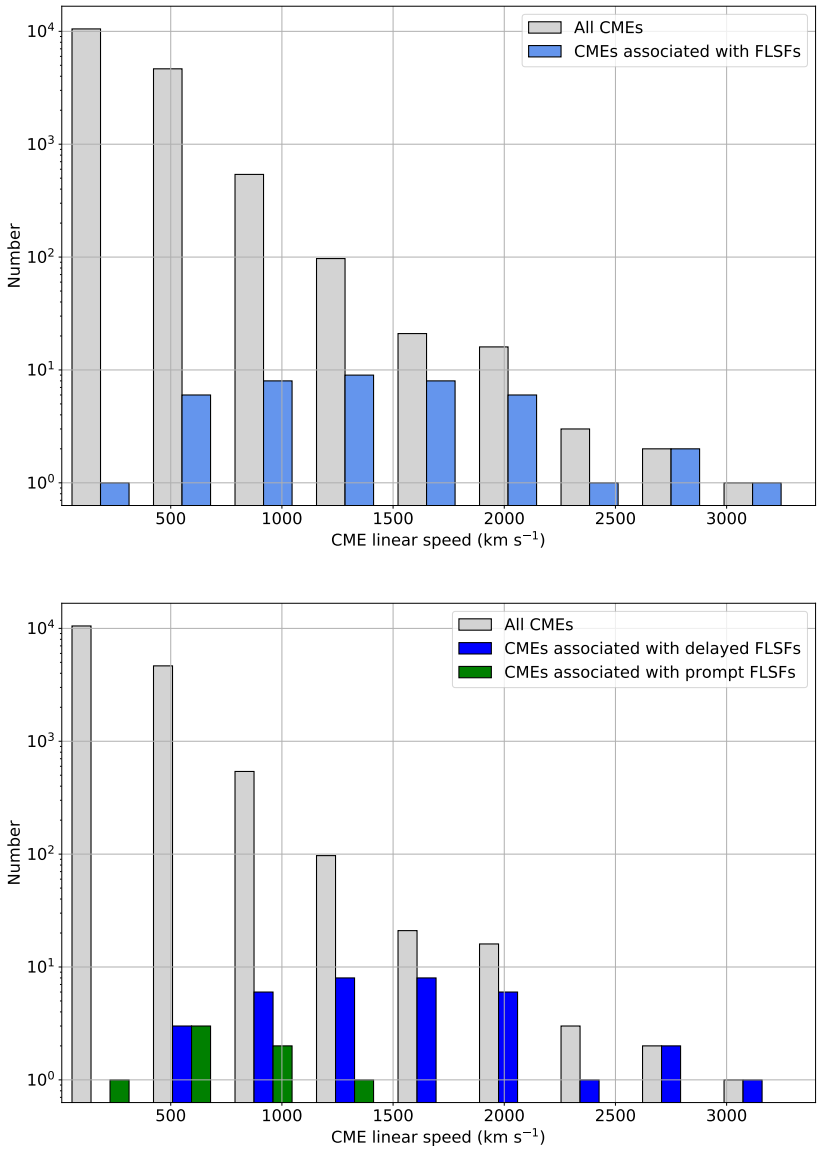

Fig. 19.— Top panel: Distribution of the CME linear speed for all of solar cycle 24 (in gray) and for all the FLSFs in this work (light blue). Bottom panel: Distribution of the CME linear speed for FLSFs classified as delayed (blue) and FLSFs classified as prompt (green). The mean speed for the *delayed* flares is 1535 km s^{-1} and for the *prompt* flares is 656 km s^{-1}. As in top panel, the gray histogram represents the CME linear speed for all of the CMEs of solar cycle 24 (whose mean speed is 342 km s^{-1}).

with speed >1200 km s^{-1}) happened in the earlier half (January 2010 – January 2014) (61 vs 35). Similar behaviour was observed for major SEP events (30 in the first half and 12 in the second half of the Cycle). Interestingly, the number of FLSFs is also larger in the first half of the Cycle, with 33 flares, while only 12 occurred in the second half. To quantify this behavior we show in Figure 20 the cumulative distributions of XRT flares and fast CME (linear speed >1000 km s^{-1}) events compared with the distribution of FLSFs. The latter seems to be in much better agreement with the distribution of fast CME events, with a Kolmogorov-Smirnov test p-value of 0.15, while the comparison of XRT flares with FLSFs gives a p-value of 4.6×10^{-4}. This result is also suggesting that high-energy solar flares have a stronger association with fast CME rather than with bright X-ray flares.

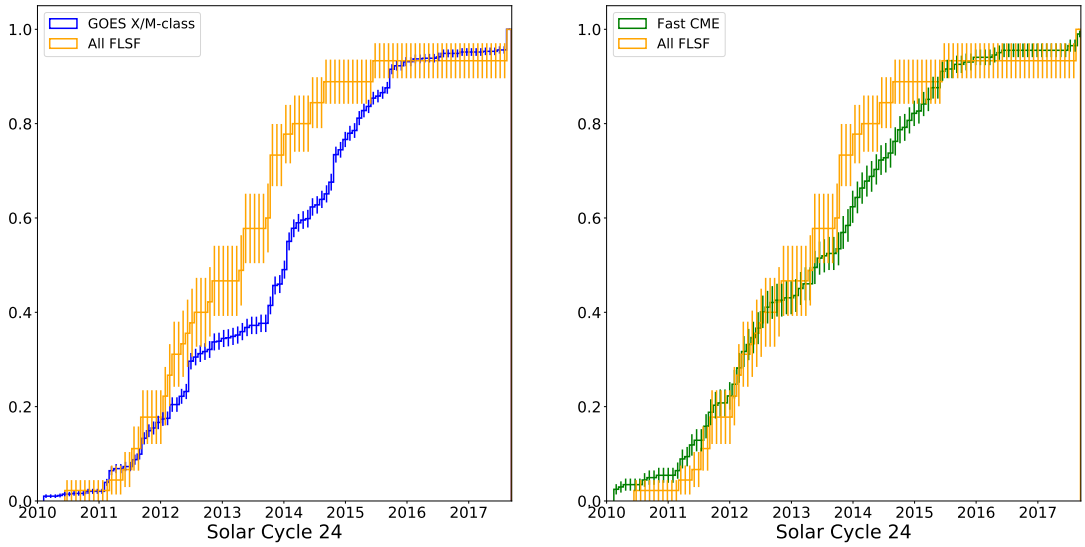

Fig. 20.— Cumulative number of FLSFs as a function of time compared with the distribution for M/X class GOES flares (left) and fast CME (linear speed >1000 km s^{-1}) events (right).

4.1. FLSF Active Region Positions

The positions on the solar surface of the ARs associated with the FLSFs are plotted together with the M/X class flares detected by Hinodes's XRT (Sakurai 2008) in Figure 21. Three BTL flares, whose position was inferred from STEREO, appear with longitudes

smaller or greater than -90° and +90°. The distribution in longitude is rather uniform, with the same number of flares in positive and negative longitudes between -90° and +90°. However, there is an asymmetry in the distributions in latitude, with a preponderance of FLSFs (∼65%) in the northern hemisphere, while the opposite is true for the XRT flares. This asymmetry is also evident in Figure 22, where we plot the positions of FLSF ARs as a function of time, illustrating the so-called Butterfly pattern, with ARs migrating toward the equator as the solar cycle evolves.

4.2. Flare Series

A notable feature of the FLSF population is that more than half (25 out of 45) are part of a cluster of flares originating from the same AR (see Table 5). It is common for an AR to be the source of several flares, but the high fraction of such clusters in the FLSF catalog might indicate that some ARs have the right conditions to be associated with the production of γ-rays. The most notable series happened during 2012-03-05 to 2012-03-10 and 2013-03-13 to 2013-03-15 each with four FLSFs. All of these flares were associated with fast CMEs, and both series produced strong and long-lasting SEP events. They all yielded delayed FLSF γ-ray emission lasting more than three hours. In addition, three of the eight flares were identified as having no >100 MeV γ-rays detected during the prompt phase; only delayed emission was detected. Only one additional flare behaved this way, FLSF 2013-04-11, that was found to have a short delayed emission and no prompt emission. This could indicate that the presence of previous SEP events and multiple fast CMEs is more important for the production of long lasting γ-ray emission than the presence of impulsive HXRs produced by high energy electrons.

4.3. Gamma-ray localization

The *Fermi*-LAT is the first telescope capable of determining the centroid of >100 MeV emission from solar flares. The position of the emission centroid on the solar disk can

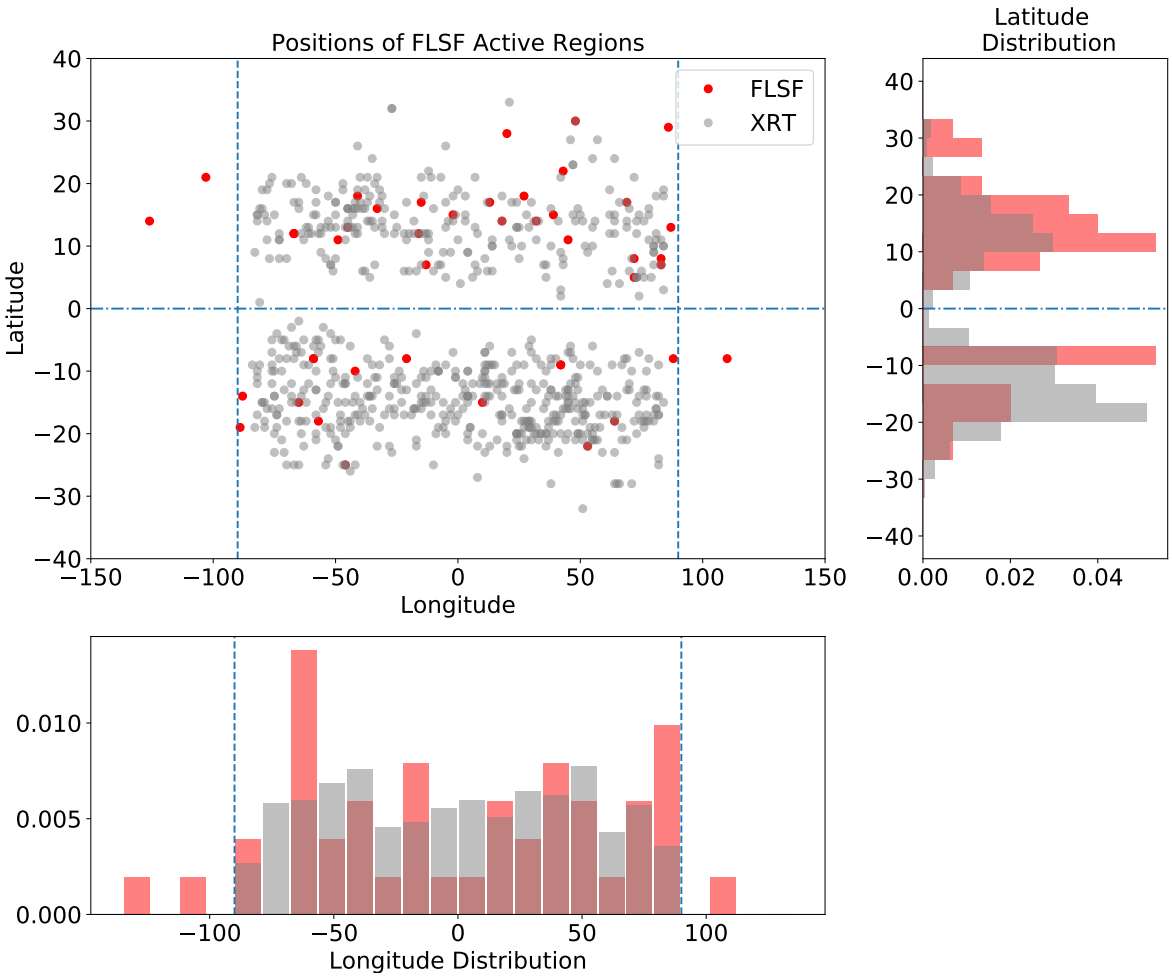

Fig. 21.— Positions of Active Regions associated with FLSFs (red) and M/X-class XRT flares (gray). Longitudes beyond -90° and +90° correspond to BTL flares. The right hand panel shows the latitude distribution of the AR positions, illustrating the asymmetry in the population. 64% of the ARs from which the FLSFs originate are located in the northern heliosphere whereas 62% of the ARs from whic the XRT flares originate are located in the southern heliosphere.

yield valuable information on where on the photosphere the precipitating ions produce the high-energy γ-rays.

For the majority of the FLSFs in the catalog, the 68% error on the emission centroid is larger than 500″ and therefore it becomes difficult to distinguish a specific region on the

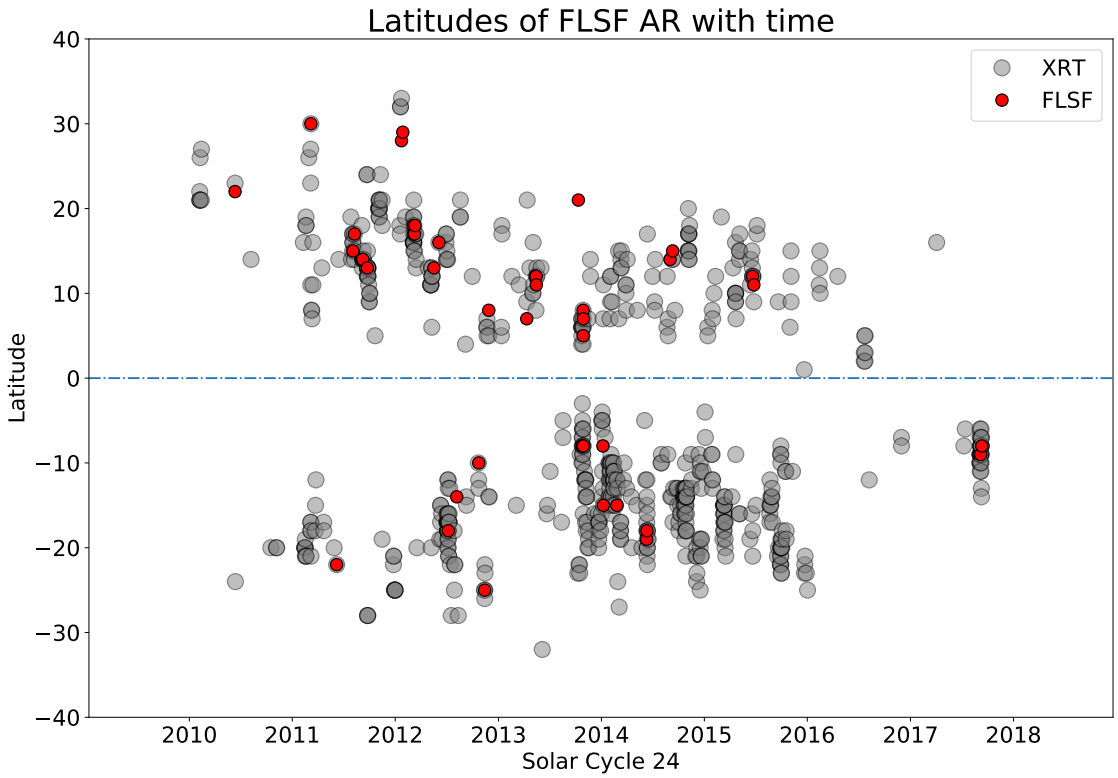

Fig. 22.— Positions of ARs associated with FLSF (red) and M/X class GOES flare (gray) as a function of time. The distribution of positions follows the so-called butterfly pattern, i.e. at the beginning of a new solar cycle, sunspots tend to form at high latitudes, but as the cycle reaches its maximum the sunspots tend to form at lower latitudes.

solar disk from which the emission is originating. For eight of the FLSFs, the 68% error radius is $\leq 365''$ (roughly a third of the solar disk), providing meaningful constraints on the location of the emission centroid that can then be compared with the lower-energy flare emission sites. The localization results for these eight flares are given in Table 6. The first eight columns of Table 6 report the date and time window of the detection, position of the centroid of the >100 MeV emission in helioprojective coordinates (X,Y), the 68% and 95% uncertainty on the emission centroid, the AR number and position, the angular distance and relative distance of the emission centroid from the AR[18]. The last column shows the

[18]The position of the AR at the time of the GOES X-ray flare

ratio of this distance to the 95% error radius. We emphasize that the position and the confidence intervals in the table are derived by modeling the high-energy emission as a point source, i.e. with no geometric extent on the solar surface.

Three of the eight flares (FLSF 2012-03-07, FLSF 2014-02-25 and FLSF 2017-09-10) were sufficiently bright and long-lasting to be localized in multiple `SunMonitor` time windows. The FLSF 2012-03-07 was an exceptional γ-ray flare in terms of both duration and brightness. The error radius was smaller than $300''$ in four detection windows, and the emission centroid moved progressively across the solar disk over the $\sim$10 hours of γ-ray emission, as shown in Figure 23. This flare was the first for which this behavior in $>$100 MeV γ-rays could be observed, and it was interpreted as supporting evidence for the CME driven shock scenario as the particle accelerator (Ajello et al. 2014). For FLSF 2014-02-25, the statistics were sufficient to provide meaningful localization in only two time intervals, and the emission centroid remained consistent with the AR position over three hours, as shown in Figure 24. Finally, FLSF 2017-09-10 was also an exceptionally bright flare, but, because the AR was located at the very edge of the western limb, it was impossible to observe any progressive motion of the γ-ray source. Throughout the 7-hour detection, the source centroid remained consistent with the AR position, as shown in Figure 25.

Two out of these eight flares originated from ARs whose position was located behind the visible solar disk, highlighting how bright these flares were regardless of the position of the AR. All eight FLSFs were classified as GOES X-class flares, with the exception of the BTL FLSF 2013-10-11 whose GOES classification of M4.9 is most likely an underestimation (Nitta et al. 2013; Pesce-Rollins et al. 2015). The peak γ-ray fluxes were all greater than 3×10^{-5} ph cm^{-2} s^{-1} and exposure times were all greater than 20 minutes, indicating that they are not impulsive flares. Five of the FLSFs originated from ARs from the eastern quadrant and three from the western quadrant of the solar disk.

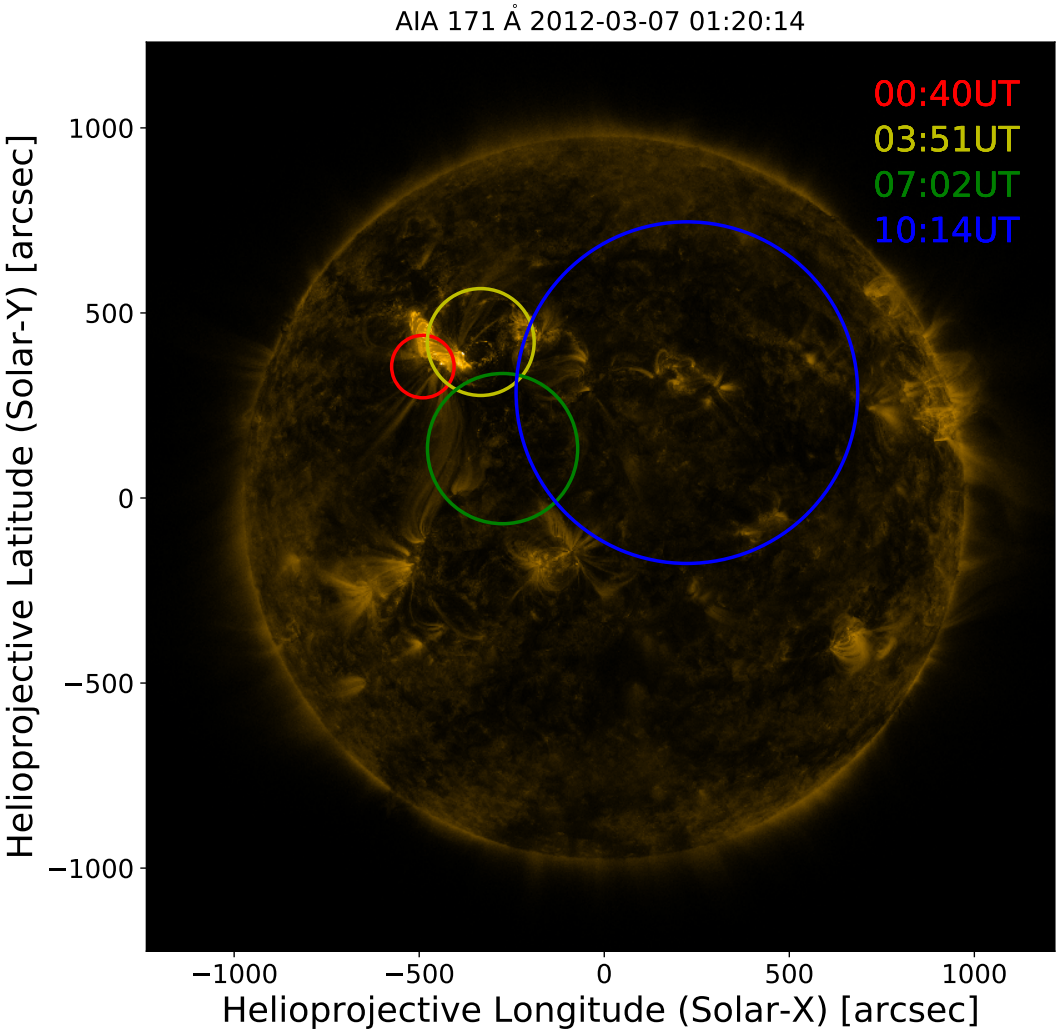

Fig. 23.— *Fermi*-LAT localization of the >100 MeV data in multiple time windows from the FLSF 2012-03-07. The error radii correspond to the 95% confidence region. The start of the time windows is annotated in the upper right corner of the figure. The localization centroid is overplotted on the AIA 171Å image of the Sun at the time of the flare.

4.4. GOES X-class flares not detected by the LAT

In an attempt to characterize the solar flares associated with γ-ray detections, we can also examine the population of solar flares not detected by the *Fermi*-LAT above 30 MeV.

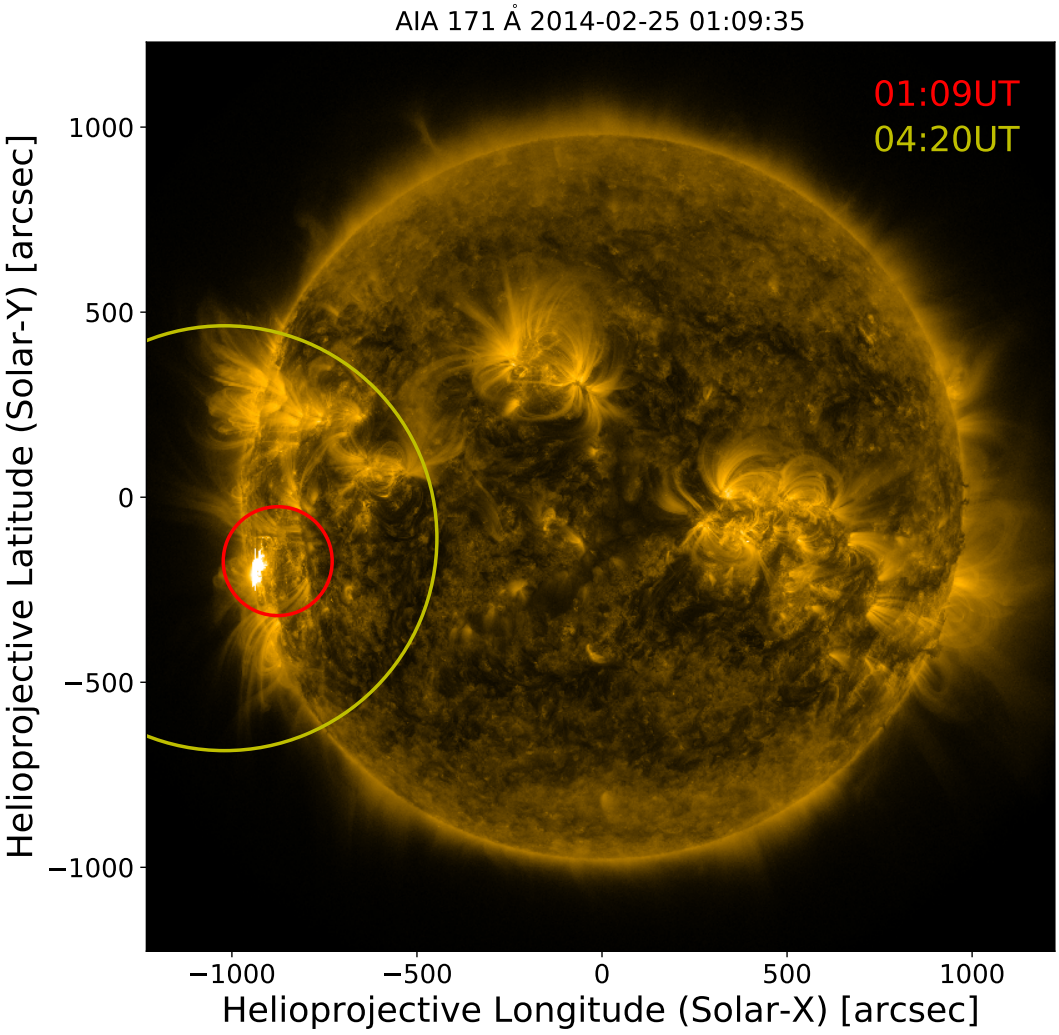

Fig. 24.— *Fermi*-LAT localization of the >100 MeV data in multiple time windows from the FLSF 2014-02-25. The error radii correspond to the 95% confidence region. The start of the time windows is annotated in the upper right corner of the figure. The localization centroid is overplotted on the AIA 171Å image of the Sun at the time of the flare.

During the time period considered in this paper, there were a total of 772 M and X class

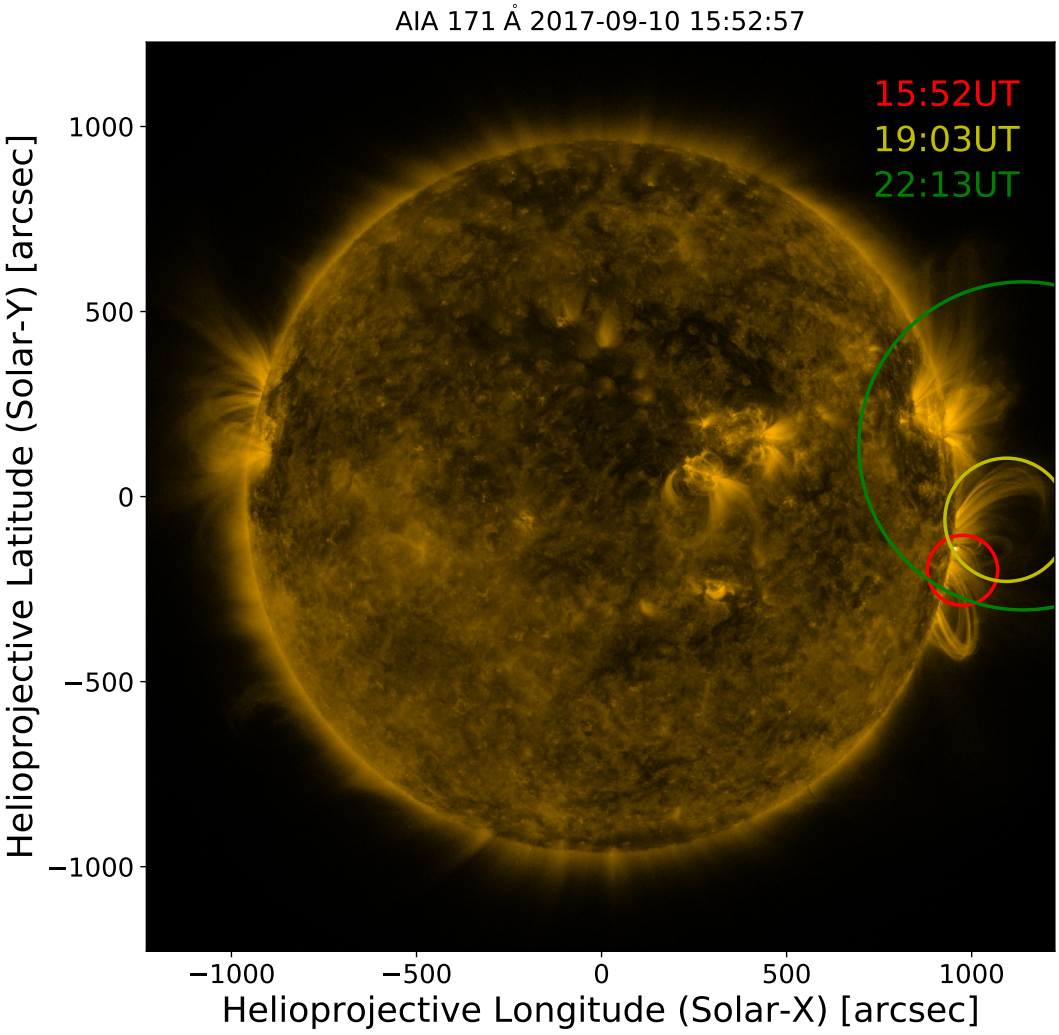

Fig. 25.— *Fermi*-LAT localization of the 100 MeV data in multiple time windows from the FLSF 2017-09-10. The error radii correspond to the 95% containment, the start of the time windows are annotated in the upper left-hand corner of the figure. The localization centroid is overplotted on the AIA 171Å image of the Sun at the time of the flare.

flares (49 were X-class flares and 24 of these were associated with FLSFs)[19]. In Table 7

[19]Here we include FLSF 2012-03-07, we associate the γ-ray emission with the X5.4 X-ray flare and with the CME with linear speed of 2684 km s^{-1}. Two of the three BTL flares have an estimated GOES class of

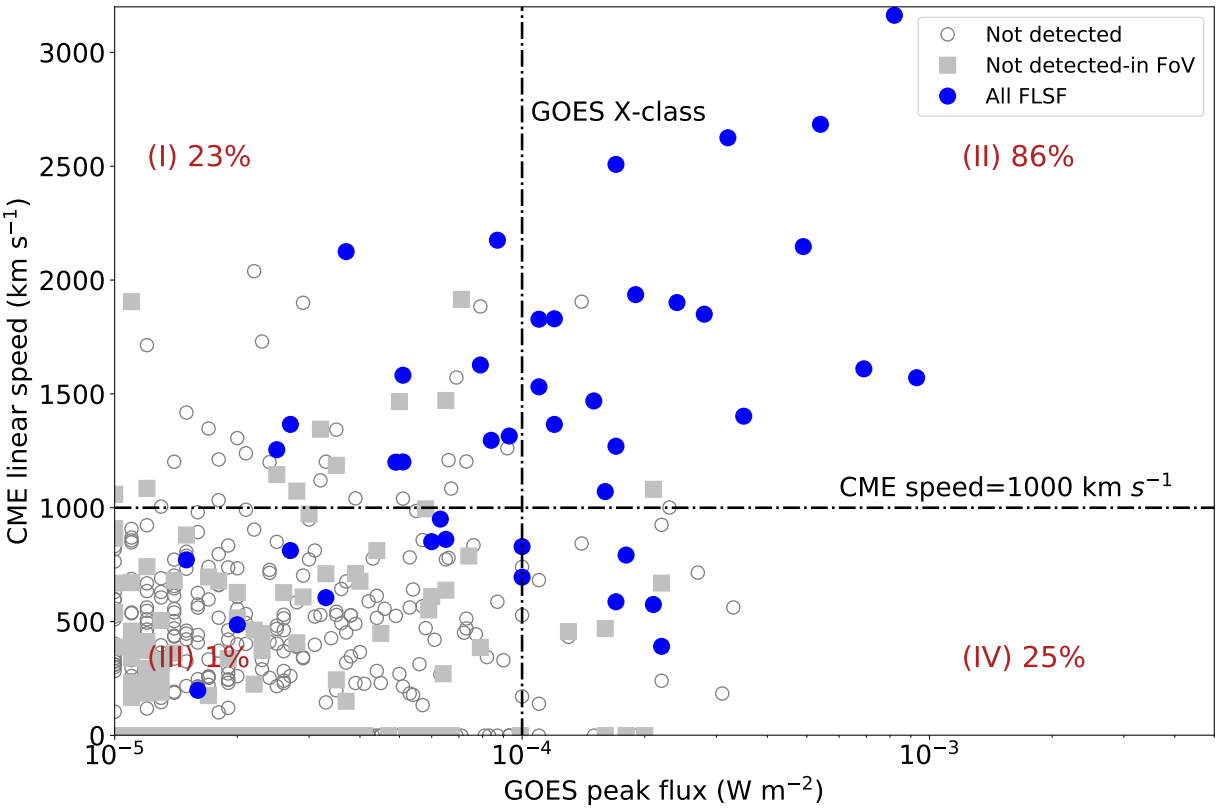

Fig. 26.— CME linear speed versus GOES peak flux for all the FLSFs (blue points), M/X-class flares not detected by the *Fermi*-LAT outside the LAT FoV (gray empty circles) and in the FoV (gray filled square) at the time of the GOES X-ray flare. The vertical dashed line indicates the border between M and X class GOES flares. The horizontal dashed line indicates a 1000 km s^{-1} CME speed. In each of the four quadrants (labeled I-IV) we indicate the fraction of flares detected by the LAT in that quadrant.

we list only the 25 X-class flares not associated with a γ-ray detection and their possible associations to CMEs and SEP events. Figure 26 shows a scatter plot of CME speed versus GOES flux for all FLSFs and all the M/X class flares non detected by the LAT. We have labeled the four quadrants (I-IV) that indicate the population of flares classified as M/X class and whether they were associated with a CME with linear speed $>$ / $<$ 1000 km

X3.5 and X2.4, but are not considered in this comparison because we do not have a catalog of X-class flares occurring behind the limb.

s^{-1}. We report the fraction of LAT detected flares over the total number of flares that fall within the quadrant. From this figure it is possible to see that most favourable condition for the LAT to detect γ-ray emission is for the flare to be of X-class and be associated with a CME with linear speed greater than 1000 km s^{-1} (86% of the flares detected by the LAT) and that the least favourable condition (1% of the flares detected by the LAT) is diagonally opposite (i.e. M class and slow CME speed). The conditions in the off diagonal quadrants appear to be equally favourable. Out of the three flares not detected by the LAT and in quadrant IV, the `SunMonitor` picked up a marginal detection in the 3 following observing windows (with a σ = 4.5, 4.0, 4.0) for the flare of 2011-09-22 that was associated with a Halo CME with a linear speed of 1905 km s^{-1}.

5. Summary and Discussion

Continuous monitoring of the Sun by *Fermi*-LAT has led to high-confidence detection of 45 solar flares with γ-ray emission above 60 MeV. With such a relatively sizable sample of flares it is now possible to perform population studies of γ-ray solar flares. Based on the temporal characteristics and associations with multiwavelegth flaring activity, we have found that there are at least two distinct types of γ-ray emission in solar flares: *prompt-impulsive* and *delayed-gradual*. Within these two broad classes we find a rich and diverse sample of events with a wide variety of characteristics. Of the 45 FLSFs discussed in this work, six have been detected only with a prompt-impulsive emission correlated with HXR emission (classified as *prompt-only*), four have no γ-ray emission detected during the impulsive HXR emission but were significantly bright after all other flare emission activities had ceased (classified as *delayed-only*), and ten have both *prompt* and *delayed* emission. For the remaining 25 flares with delayed emission, we cannot exclude the presence of *prompt* emission because the Sun was not in the FoV of the LAT during the impulsive HXR activity phase.

The most significant results presented in this work can be summarized as follows:

1. Emission above 60 MeV could be due to bremsstrahlung radiation produced by electrons of Lorentz factor $\gamma_e > 100$ with relatively hard spectrum is most probably an unlikely scenario. This is because the acceleration of electrons to such energies is difficult due to high synchrotron losses. We find that emission due to decay of pions ($\pi^0, \pi^{\pm}$) produced by > 300 MeV protons and ions, with a power law spectrum of index $\sim 4 - 5$, extending up to 10s of GeV, produces very good fit to all observed γ rays.

2. All of the FLSFs with LLE *prompt* emission (produced by > 300 MeV ions) reach their peak within seconds of the 100–300 keV emission peak (produced by > 100 keV electrons) observed with *Fermi*-GBM implying that these ions and electrons are accelerated, transported, and interact with the ambient medium at the same time. Similar conclusions for acceleration of lower energy (1 to 30 MeV) ions were reached by Chupp (1987) and Hurford et al. (2006) based on the *RHESSI* imaging of the 2.223 MeV neutron-capture γ-ray line, and by Shih et al. (2009) who reported a tight correlation between the 2.223 MeV line fluence and the >300 keV electron bremsstrahlung fluence.

3. All but three of the flares in the FLSF catalog are associated with CMEs. The *delayed* type flares are associated with faster CMEs (mean speed of 1535 $\mathrm{km\,s^{-1}}$) whereas the *prompt* type FLSFs are associated with slower CMEs (mean speed of 656 $\mathrm{km\,s^{-1}}$).

4. One of the most important contribution of *Fermi*-LAT has been its ability to localize the centroids of high-energy γ-ray emission on the Sun. In most such cases the initial centroid position is at or near the AR where the flare originated. In several long lasting strong flares there are clear indications of change of the centroid position with time; often away from the AR. This change is best observed in the strong, long-lasting FLSF 2012-03-07, where the centroid of >100 MeV emission gradually migrates away from the AR up to tens of degrees. This indicates that the acceleration site of the γ-ray producing high energy ions is magnetically connected to regions on the photosphere far away from the initial AR.

5. Further evidence for this scenario comes from, for the first time, *Fermi* observation of GeV emission from three behind-the-limb flares including two-hour emission from FLSF 2014-09-01 originating 40 degrees behind the limb. Localization of the γ-ray emission from two of these flares indicates that the emission occurred on the visible disk, again necessitating a way for the ions from the acceleration site to access regions on the visible disk (more than 40 degrees away from the AR) to interact and to produce the observed γ-rays. Similar conclusions were also reached by Cliver et al. (1993) and Vestrand & Forrest (1993) for the observations with CGRO-EGRET of behind-the-limb flares with emission up to 100 MeV.

6. There is an asymmetry in the latitude distribution of the ARs from which the FLSFs originate, with 65% of the flares coming from the northern heliosphere. The opposite is true for the M/X-class XRT flares detected during the same time interval. Shrivastava & Singh (2005) found that CMEs associated with Forbush decreases also come predominately from the northern heliosphere.

7. More than half of the FLSFs in this catalog are part of a series of flare clusters. The most notable clusters happened from 2012-03-05 to 2012-03-10 and from 2013-05-13 to 2013-05-15 with each consisting of four FLSFs. All of these flares were associated with fast CMEs, and both series produced strong and long-lasting SEP events. They all yielded delayed FLSF γ-ray emission lasting more than three hours. In addition, three of these eight flares showed no impulsive phase γ-ray emission (only one other non-series FLSF was found with similar properties). This could suggest that the presence of previous SEP events and multiple fast CMEs is more important for production of long lasting γ-ray emission than the presence of impulsive HXRs produced by high-energy electrons.

8. Seven FLSFs in the catalog are detected with both LLE-prompt and delayed phases, with the average peak flux of the prompt phase 10 times higher than that of the delayed phase. However, the total energy released during the delayed phase is 10–100 times larger than that during the prompt phase.

Solar eruptive events involve two distinct but related phenomena: (1) acceleration of electrons and ions at the reconnection regions in coronal loops that produce the impulsive nonthermal radiation observed from microwaves to γ rays, lasting several minutes, and are observed as impulsive-prompt SEPs, often with substantial enhanced abundances of ^{3}He and heavier ions. (2) production of a supersonic CME which drives a shock, where particles are accelerated resulting in long-duration SEPs with normal ionic abundances, with only one radiative signature of type II radio emission produced by less numerous SEP electrons. As summarized above, the *Fermi*-LAT observations show both prompt-impulsive γ-ray emission having light curves similar to those of the HXRs, and long-duration delayed emission with temporal behavior similar to SEPs, and like gradual SEPs, associated with fast CMEs. These similarities between gradual SEPs and > 60 MeV gradual-delayed emission, plus the observed drifting of the centroid of γ-ray emission from the original active region, which is accentuated by the observations of behind-the-limb flares, indicate that the site and mechanism of the acceleration of ions responsible for the long duration γ rays is different than that of particles producing the impulsive nonthermal flare radiation, and suggest that long duration γ rays are another radiative signature of acceleration in CME-shocks. However, unlike the type II radiation they are produced by ions (accelerated in the CME driven shock) and not in the low density environment of the CME. While SEPs are particles escaping the upstream of the shock, the γ rays must be produced by ions escaping from downstream region of the shock back to the high density photosphere of the Sun, and because of complex and changing magnetic connection between the CME and the Sun, sometimes to regions far from the AR from which the eruptions originated. Recent reconstruction of these magnetic connections by Jin et al. (2018) provide support for this scenario.

Alternative scenarios for explaining the gradual-delayed emission observed by *Fermi* have been put forth by authors such as De Nolfo et al. (2019) in their comparison between the characteristics of high-energy SEPs observed by PAMELA and those of the *delayed*-type emission γ-ray flares. One such scenario is that particles are accelerated via the second-order

Fermi mechanism and trapped locally within extended coronal loops. These accelerated particles would then diffuse to the denser photosphere to radiate (Ryan & Lee 1991). With this approach it is possible to decouple the acceleration of the particles producing γ rays from the acceleration and transport of the SEPs, allowing for different energetic particle productivities.

Thanks to the increase in sensitivity of the *Fermi*-LAT the sample of > 100 MeV γ-ray flares has increased by almost a factor of 10 thus allowing to perform population studies on these events for the first time. The observations presented in this work suggest that the particles producing the *prompt*-type emission and those producing the *delayed*-type emission are accelerated via different mechanisms. However, further multiwavelength observations and in-depth simulations are needed in order to come to a definitive answer to which acceleration mechanism is driving the *delayed*-type γ-ray emission of solar flares.

The *Fermi* LAT Collaboration acknowledges generous ongoing support from a number of agencies and institutes that have supported both the development and the operation of the LAT as well as scientific data analysis. These include the National Aeronautics and Space Administration and the Department of Energy in the United States, the Commissariat à l'Energie Atomique and the Centre National de la Recherche Scientifique / Institut National de Physique Nucléaire et de Physique des Particules in France, the Agenzia Spaziale Italiana and the Istituto Nazionale di Fisica Nucleare in Italy, the Ministry of Education, Culture, Sports, Science and Technology (MEXT), High Energy Accelerator Research Organization (KEK) and Japan Aerospace Exploration Agency (JAXA) in Japan, and the K. A. Wallenberg Foundation, the Swedish Research Council and the Swedish National Space Board in Sweden.

Additional support for science analysis during the operations phase is gratefully acknowledged from the Istituto Nazionale di Astrofisica in Italy and the Centre National d'Études Spatiales in France. This work performed in part under DOE Contract DE-AC02-76SF00515.

MPR and NO acknowledge relevant and helpful discussions with members of the ISSI International Team on Energetic Ions: The Elusive Component of Solar Flares and with participants in the Lorentz Center Workshop on Solar Sources of GeV Gamma-rays, 26 Feb - 2 Mar 2018.

Name	GOES Class	GOES Start-Stop	Detection duration (hrs)	Total duration (hrs)	Peak Flux (10^{-5}cm^{-2}s^{-1})	Fluence > 100 MeV (cm^{-2})	Flare Type	Total Protons >500 MeV (10^{27})
FLSF 2011-03-07	M3.7[c]	19:43 - 20:58	13.5	15.8 ± 3.1	3.23 ± 0.22	1.076 ± 0.029	Delayed	64.4 ± 1.8
FLSF 2011-06-07	M2.5	06:16 - 06:59	3.8	6.0 ± 2.2	3.18 ± 0.20	0.295 ± 0.030	Delayed	19.5 ± 2.0
FLSF 2011-08-04	M9.3	03:41 - 04:04	0.7	2.3 ± 0.7	2.30 ± 0.18	0.13 ± 0.05	Delayed	9 ± 4
FLSF 2011-08-09	X6.9	07:48 - 08:08	0.5	0.87 ± 0.34	2.29 ± 0.23	0.037 ± 0.018	Prompt Short-Delayed[a]	2.7 ± 1.3
FLSF 2011-09-06	X2.1	22:12 - 22:24	0.6	2.0 ± 1.4	22.8 ± 0.4	0.87 ± 0.17	LLE-Prompt Short-Delayed[a]	58 ± 12
FLSF 2011-09-07	X1.8	22:32 - 22:44	0.8	2.02 ± 0.35	0.77 ± 0.08	0.041 ± 0.014	Delayed	2.3 ± 0.7
FLSF 2011-09-24	X1.9	09:21 - 09:48	0.5	1.2 ± 0.7	0.50 ± 0.10	0.014 ± 0.007	LLE-Prompt Short-Delayed[a]	-
FLSF 2012-01-23	M8.7	03:38 - 04:34	5.3	5.9 ± 1.0	1.99 ± 0.12	0.340 ± 0.014	Delayed	24.7 ± 1.0
FLSF 2012-01-27	X1.7	17:37 - 18:56	5.3	6.8 ± 1.5	3.3 ± 0.5	0.248 ± 0.025	Delayed	17.2 ± 1.8
FLSF 2012-03-05	X1.1	02:30 - 04:43	3.8	4.4 ± 1.2	0.63 ± 0.07	0.085 ± 0.007	Delayed	6.1 ± 0.5
FLSF 2012-03-07	X5.4[c]	00:02 - 00:40	19.6	20.3 ± 0.8	233 ± 8	33.996 ± 0.030	Delayed	1844.7 ± 1.3
FLSF 2012-03-09	M6.3	03:22 - 04:18	5.5	7.2 ± 1.7	0.96 ± 0.12	0.148 ± 0.007	No-Prompt Delayed	9.29 ± 0.23
FLSF 2012-03-10	M8.4	17:15 - 18:30	2.3	6 ± 4	0.23 ± 0.06	0.042 ± 0.012	Delayed	2.3 ± 0.6
FLSF 2012-05-17	M5.1	01:25 - 02:14	2.1	2.6 ± 0.5	1.19 ± 0.19	0.0572 ± 0.0026	Delayed	2.29 ± 0.09
FLSF 2012-06-03	M3.3	17:48 - 17:57	0.4	1.9 ± 1.5	3.06 ± 0.25	0.117 ± 0.031	LLE-Prompt Short-Delayed[a]	7.7 ± 2.0
FLSF 2012-07-06	X1.1	23:01 - 23:14	0.8	1.27 ± 0.35	3.06 ± 0.15	0.100 ± 0.021	Delayed	7.5 ± 1.6
FLSF 2012-10-23	X1.8	03:13 - 03:21	0.5	1.9 ± 0.5	0.73 ± 0.18	0.047 ± 0.018	LLE-Prompt Delayed[a]	-
FLSF 2012-11-13	M6.0	01:58 - 02:04	0.7	0.041 ± 0.006	0.46 ± 0.09	0.006 ± 0.022	Prompt	-
FLSF 2012-11-27	M1.6	15:52 - 16:03	0.8	0.166 ± 0.025	0.27 ± 0.07	0.005 ± 0.030	Prompt Short-Delayed	-
FLSF 2013-04-11	M6.5	06:55 - 07:29	0.7	0.38 ± 0.27	5.71 ± 0.24	0.099 ± 0.016	No-Prompt Short-Delayed	6 ± 6
FLSF 2013-05-13a	X1.7	01:53 - 02:32	0.7	4.0 ± 1.3	0.96 ± 0.11	0.11 ± 0.06	Delayed	8 ± 5
FLSF 2013-05-13b	X2.8	15:48 - 16:16	3.9	6.1 ± 2.2	2.41 ± 0.21	0.35 ± 0.04	Delayed	19.7 ± 2.3
FLSF 2013-05-14	X3.2	00:00 - 01:20	5.6	5.9 ± 0.5	3.30 ± 0.15	0.401 ± 0.004	No-Prompt Delayed	27.82 ± 0.28
FLSF 2013-05-15	X1.2	01:25 - 01:58	0.8	3.5 ± 0.5	0.36 ± 0.07	0.052 ± 0.023	No-Prompt Delayed	-
FLSF 2013-10-11	M4.9*	07:01 - 07:45	0.7	0.38 ± 0.32	12.5 ± 0.4	0.262 ± 0.013	BTL Short-Delayed	9 ± 9
FLSF 2013-10-25a	X1.7	07:53 - 08:09	0.7	1.4 ± 0.5	1.15 ± 0.12	0.042 ± 0.013	Delayed	3.3 ± 1.0
FLSF 2013-10-28c	M2.7[c]	14:46 - 15:04	0.3	1.6 ± 0.6	0.81 ± 0.12	0.036 ± 0.014	Delayed	-
FLSF 2014-01-06	X3.5*	07:40 - 08:08	0.6	0.27 ± 0.04	0.42 ± 0.09	0.0061 ± 0.0028	BTL Short-Delayed	0.31 ± 0.31
FLSF 2014-01-07	X1.2	18:04 - 18:58	0.8	1.05 ± 0.26	0.29 ± 0.07	0.0081 ± 0.0020	Delayed	-
FLSF 2014-02-25	X4.9	00:39 - 01:03	6.7	8.4 ± 1.8	169.6 ± 2.0	13.95 ± 0.18	LLE-Prompt Delayed[a]	719 ± 8
FLSF 2014-06-10	X1.5	12:36 - 13:03	0.4	1.9 ± 0.6	1.17 ± 0.26	0.064 ± 0.026	LLE-Prompt Delayed[a]	-
FLSF 2014-06-11	X1.0	08:59 - 09:10	0.4	0.23 ± 0.17	0.99 ± 0.26	0.007 ± 0.005	Short-Delayed	-
FLSF 2014-09-01	X2.4*	10:58 - 11:40	1.9	2.5 ± 1.2	379 ± 7	12.1 ± 2.3	BTL Delayed	$(7.4 \pm 1.4) \times 10^2$
FLSF 2014-09-10	X1.6	17:21 - 18:20	0.3	0.30 ± 0.06	7.4 ± 0.5	0.172 ± 0.012	Short-Delayed	5 ± 5
FLSF 2015-06-21	M2.7[c]	02:04 - 03:15	10.1	11.5 ± 2.5	1.26 ± 0.15	0.296 ± 0.011	Prompt Delayed	16.7 ± 0.7
FLSF 2015-06-25	M7.9	08:02 - 09:05	0.7	2.4 ± 1.3	0.40 ± 0.08	0.030 ± 0.004	Delayed	2.28 ± 0.29
FLSF 2017-09-06a	X2.2	08:57 - 09:17	0.5	0.169 ± 0.025	1.31 ± 0.16	0.020 ± 0.007	Prompt	0.6 ± 0.6
FLSF 2017-09-06b	X9.3[c]	11:53 - 12:10	13.0	13.33 ± 0.32	3.6 ± 0.5	1.0700 ± 0.0022	Delayed	79.41 ± 0.13
FLSF 2017-09-10	X8.2	15:35 - 16:31	13.3	13.9 ± 1.2	291.0 ± 2.1	22.2 ± 1.6	Prompt Delayed[a]	$(9.5 \pm 0.7) \times 10^2$

Table 1: FLSF catalog for flares detected with the *Fermi*-LAT `SunMonitor` and their likely GOES X-ray flare associations. In the *GOES*-class column entries with a $*$ identify the BTL flares, whose class is estimated based on the STEREO observation, and [a] indicate that there is also a LLE detection of the flare. The analysis results for the LLE flares are shown in Table 3.

Date and Time (UTC)	Exposure (minutes)	Flux (10^{-5} ph cm^{-2}s^{-1})	TS	ΔTS	Model	Photon Index	Cutoff Energy (MeV)	Proton index
2011-03-07 20:10 - 20:39	29	2.06 ± 0.19	317	27	Exp	-0.76 ± 0.45	172 ± 55	4.3 ± 0.4
2011-03-07 23:21 - 00:05	44	3.04 ± 0.20	710	70	Exp	-0.31 ± 0.36	138 ± 27	4.13 ± 0.26
2011-03-08 02:33 - 03:16	43	3.23 ± 0.22	621	66	Exp	-0.15 ± 0.41	110 ± 22	4.70 ± 0.32
2011-03-08 05:44 - 06:27	44	1.40 ± 0.15	219	32	Exp	0.67 ± 0.99	63 ± 22	>6
2011-03-08 09:13 - 09:39	26	0.48 ± 0.11	46	-0.1	PL	-2.55 ± 0.25	-	-
2011-06-07 07:47 - 08:23	36	3.18 ± 0.20	740	76	Exp	-0.13 ± 0.37	104 ± 19	4.97 ± 0.33
2011-06-07 11:16 - 11:34	19	0.32 ± 0.10	19	5	PL	-2.70 ± 0.35	-	-
2011-08-04 04:55 - 05:37	42	2.30 ± 0.18	413	49	Exp	-0.09 ± 0.50	95 ± 21	5.4 ± 0.4
2011-08-09 07:37 - 08:09	32	2.29 ± 0.23 *	186	26	Exp	-0.04 ± 0.87	91 ± 37	5.4 ± 0.6
2011-09-06 22:11 - 22:47	36	22.8 ± 0.4 *	8197	437	Exp	-0.89 ± 0.09	161 ± 11	4.89 ± 0.11
2011-09-07 23:35 - 00:23	48	0.77 ± 0.08	270	30	Exp	-0.10 ± 0.69	114 ± 40	4.4 ± 0.5
2011-09-24 09:18 - 09:47	30	0.50 ± 0.10 *	50	5	PL	-2.51 ± 0.22	-	-
2012-01-23 04:06 - 04:46	40	1.12 ± 0.11	258	26	Exp	0.12 ± 1.09	81 ± 40	5.5 ± 0.6
2012-01-23 05:33 - 06:21	48	1.99 ± 0.12	796	92	Exp	0.25 ± 0.41	80 ± 13	5.6 ± 0.4
2012-01-23 07:20 - 07:47	27	1.97 ± 0.31	93	12	Exp	-0.25 ± 1.05	100 ± 49	5.5 ± 0.9
2012-01-23 08:58 - 09:26	28	1.63 ± 0.23	116	27	Exp	1.81 ± 1.41	51 ± 18	5.6 ± 0.8
2012-01-27 19:37 - 19:55	18	3.3 ± 0.5	102	14	Exp	0.31 ± 1.43	65 ± 33	>6
2012-01-27 21:08 - 21:36	28	0.72 ± 0.14	66	8	PL	-2.53 ± 0.20	-	-
2012-01-28 00:19 - 00:55	36	0.25 ± 0.09	19	1	PL	-2.60 ± 0.39	-	-
2012-03-05 04:07 - 04:49	42	0.58 ± 0.09	100	11	Exp	0.34 ± 1.33	63 ± 31	>6
2012-03-05 05:36 - 06:24	48	0.63 ± 0.07	175	16	Exp	-0.20 ± 0.85	79 ± 31	>6

Continued on next page

Date and Time (UTC)	Exposure (minutes)	Flux (10^{-5} ph cm^{-2}s^{-1})	TS	ΔTS	Model	Photon Index	Cutoff Energy (MeV)	Proton index
2012-03-05 07:18 - 07:54	36	0.55 ± 0.11	53	6	PL	-2.52 $\pm$ 0.21	-	-
2012-03-07 00:40 - 01:20	40	233 ± 8 *	75611	-254574	Exp	-0.65 $\pm$ 0.03	182 $\pm$ 4	3.875 ± 0.025
2012-03-07 02:26 - 02:45	18	75.1 ± 2.6	2377	117	Exp	-1.45 $\pm$ 0.13	355 $\pm$ 47	3.77 ± 0.10
2012-03-07 03:51 - 04:31	40	95.1 ± 1.2	21100	1459	Exp	-0.84 $\pm$ 0.05	199 $\pm$ 8	4.01 ± 0.05
2012-03-07 05:38 - 05:55	18	97.3 ± 3.2	2675	249	Exp	-0.59 $\pm$ 0.17	147 $\pm$ 14	4.51 ± 0.13
2012-03-07 07:02 - 07:42	40	62.8 ± 1.0	12829	1210	Exp	-0.30 $\pm$ 0.08	120 $\pm$ 5	4.71 ± 0.07
2012-03-07 08:49 - 09:06	17	49.8 ± 2.5	1181	123	Exp	-0.17 $\pm$ 0.32	102 $\pm$ 14	5.17 ± 0.24
2012-03-07 10:14 - 10:54	25	26.8 ± 0.9	2803	344	Exp	0.27 $\pm$ 0.21	84 $\pm$ 7	5.28 ± 0.17
2012-03-07 13:24 - 14:04	13	8.6 ± 0.9	258	31	Exp	0.30 $\pm$ 0.75	78 $\pm$ 22	5.7 ± 0.6
2012-03-07 16:35 - 16:48	13	1.54 ± 0.32	49	10	Exp	1.41 $\pm$ 1.91	46 $\pm$ 23	>6
2012-03-07 18:23 - 18:32	9	2.2 ± 0.7	25	8	PL	-2.91 $\pm$ 0.41	-	-
2012-03-07 19:46 - 20:15	29	0.26 ± 0.08	22	3	PL	-2.37 $\pm$ 0.30	-	-
2012-03-09 05:12 - 05:55	43	0.27 ± 0.08	32	-0.2	PL	-2.24 $\pm$ 0.25	-	-
2012-03-09 06:47 - 07:30	43	0.96 ± 0.12	139	20	Exp	0.09 $\pm$ 0.92	87 $\pm$ 34	5.5 ± 0.7
2012-03-09 08:22 - 09:05	43	0.89 ± 0.12	140	28	Exp	1.78 $\pm$ 1.21	50 $\pm$ 15	5.6 ± 0.8
2012-03-09 09:58 - 10:41	22	0.43 ± 0.13	25	0.3	PL	-2.51 $\pm$ 0.32	-	-
2012-03-10 21:00 - 21:34	34	0.23 ± 0.06	25	2	PL	-2.50 $\pm$ 0.30	-	-
2012-03-10 22:35 - 23:15	40	0.19 ± 0.06	18	3	PL	-3.04 $\pm$ 0.40	-	-
2012-05-17 02:12 - 02:44	32	1.19 ± 0.19	100	10	Exp	-0.72 $\pm$ 0.77	207 $\pm$ 117	3.7 ± 0.5
2012-05-17 03:49 - 04:18	30	0.44 ± 0.13	29	7	PL	-2.30 $\pm$ 0.28	-	-
2012-06-03 17:38 - 18:02	24	3.06 ± 0.25	395	39	Exp	-0.19 $\pm$ 0.63	104 $\pm$ 34	5.0 ± 0.4
2012-07-06 23:20 - 00:08	48	3.06 ± 0.15	1173	143	Exp	0.40 $\pm$ 0.35	74 $\pm$ 10	5.75 ± 0.29

Continued on next page

Date and Time (UTC)	Exposure (minutes)	Flux (10^{-5} ph cm^{-2}s^{-1})	TS	ΔTS	Model	Photon Index	Cutoff Energy (MeV)	Proton index
2012-10-23 04:13 - 04:43	30	0.73 ± 0.18	39	9	PL	-2.73 ± 0.27	-	-
2012-11-13 01:34 - 02:14	40	0.46 ± 0.09 *	60	7	PL	-2.61 ± 0.21	-	-
2012-11-27 15:48 - 16:34	46	0.27 ± 0.07	44	2	PL	-2.22 ± 0.21	-	-
2013-04-11 07:00 - 07:39	39	5.71 ± 0.24 *	1422	120	Exp	-0.43 ± 0.27	105 ± 15	5.67 ± 0.27
2013-05-13 17:15 - 17:58	30	2.41 ± 0.21	371	43	Exp	-0.24 ± 0.48	142 ± 38	3.91 ± 0.31
2013-05-13 20:26 - 21:09	43	1.72 ± 0.14	371	43	Exp	0.21 ± 0.73	80 ± 25	5.5 ± 0.5
2013-05-13 04:31 - 05:14	43	0.96 ± 0.11	188	36	Exp	3.00 ± 0.14	31 ± 2	>6
2013-05-14 01:08 - 01:55	47	1.02 ± 0.09 *	292	46	Exp	0.55 ± 0.67	65 ± 15	>6
2013-05-14 02:43 - 03:31	47	3.30 ± 0.15	1518	193	Exp	0.62 ± 0.32	77 ± 9	4.95 ± 0.24
2013-05-14 04:19 - 05:06	47	2.32 ± 0.16	546	87	Exp	1.26 ± 0.61	54 ± 9	5.9 ± 0.4
2013-05-14 05:59 - 06:42	42	0.59 ± 0.09	105	19	Exp	1.05 ± 1.43	54 ± 24	>6
2013-05-15 04:12 - 04:58	46	0.36 ± 0.07	51	9	PL	-2.62 ± 0.22	-	-
2013-10-11 06:56 - 07:39	42	12.5 ± 0.4	3949	317	Exp	-0.34 ± 0.16	131 ± 12	4.33 ± 0.12
2013-10-25 08:15 - 08:57	42	1.15 ± 0.12 *	211	21	Exp	0.07 ± 0.88	79 ± 30	6 ± 4
2013-10-28 15:45 - 16:05	21	0.81 ± 0.12	120	8	PL	-2.32 ± 0.15	-	-
2014-01-06 07:55 - 08:30	34	0.42 ± 0.09	52	13	Exp	1.84 ± 2.16	49 ± 26	5.8 ± 1.9
2014-01-07 18:41 - 19:29	48	0.29 ± 0.07	32	5	PL	-2.68 ± 0.27	-	-
2014-02-25 01:09 - 01:29	20	169.6 ± 2.0 *	24030	2121	Exp	-0.33 ± 0.06	154 ± 5	3.78 ± 0.04
2014-02-25 04:20 - 04:40	20	28.3 ± 0.9	2707	370	Exp	1.17 ± 0.28	47 ± 4	>6

Continued on next page

Date and Time (UTC)	Exposure (minutes)	Flux (10^{-5} ph cm^{-2}s^{-1})	TS	ΔTS	Model	Photon Index	Cutoff Energy (MeV)	Proton index
2014-02-25 07:30 - 07:51	21	0.87 ± 0.17	74	11	Exp	2.39 ± 2.53	29 ± 14	>6
2014-06-10 14:00 - 14:26	25	1.17 ± 0.26	49	5	PL	-2.47 ± 0.22	-	-
2014-06-11 09:06 - 09:30	24	0.99 ± 0.26 *	30	3	PL	-2.77 ± 0.30	-	-
2014-09-01 11:02 - 11:18	16	379 ± 7	41620	-5590	Exp	-1.03 ± 0.09	177 ± 10	4.70 ± 0.07
2014-09-01 12:25 - 12:57	32	2.98 ± 0.22	545	31	Exp	-1.16 ± 0.29	290 ± 82	3.72 ± 0.24
2014-09-10 17:35 - 17:53	18	7.4 ± 0.5 *	559	66	Exp	0.35 ± 0.54	86 ± 20	4.66 ± 0.34
2015-06-21 02:09 - 02:42	33	0.25 ± 0.08	23	5	PL	-3.05 ± 0.39	-	-
2015-06-21 05:19 - 05:53	33	1.26 ± 0.15	162	16	Exp	-0.18 ± 0.74	118 ± 44	4.3 ± 0.6
2015-06-21 08:30 - 09:03	33	0.81 ± 0.13	101	12	Exp	0.03 ± 1.14	110 ± 57	4.2 ± 0.7
2015-06-21 11:40 - 12:14	33	0.38 ± 0.10	31	10	Exp	2.05 ± 2.61	49 ± 29	>6
2015-06-25 09:24 - 10:09	45	0.40 ± 0.08	48	6	PL	-2.72 ± 0.22	-	-
2017-09-06 12:10 - 12:35	25	0.96 ± 0.11 *	156	17	Exp	0.05 ± 1.06	58 ± 23	>6
2017-09-06 13:23 - 14:10	26	2.63 ± 0.17 *	604	66	Exp	0.39 ± 0.55	60 ± 12	>6
2017-09-06 15:03 - 15:40	18	2.9 ± 0.4	137	24	Exp	1.20 ± 1.29	59 ± 23	5.6 ± 0.8
2017-09-06 16:45 - 17:09	19	3.6 ± 0.5	130	24	Exp	1.24 ± 1.24	64 ± 22	5.2 ± 0.7
2017-09-06 18:14 - 18:50	36	2.73 ± 0.24	337	49	Exp	0.67 ± 0.68	71 ± 17	5.4 ± 0.5
2017-09-06 19:55 - 20:20	25	2.27 ± 0.35	96	17	Exp	0.74 ± 1.33	65 ± 27	>6
2017-09-06 21:25 - 22:00	35	2.56 ± 0.24	318	36	Exp	0.11 ± 0.67	84 ± 24	5.5 ± 0.5
2017-09-06 23:05 - 23:31	26	0.96 ± 0.22	43	4	PL	-3.06 ± 0.30	-	-
2017-09-07 00:36 - 01:11	35	0.62 ± 0.13	52	4	PL	-2.63 ± 0.22	-	-
2017-09-06 08:51 - 09:19	28	1.31 ± 0.16 *	130	21	Exp	0.59 ± 1.05	60 ± 22	>6
2017-09-10 15:52 - 16:28	35	291.0 ± 2.1 *	61725	4429	Exp	-0.67 ± 0.03	195 ± 4	3.737 ± 0.026

Continued on next page

Date and Time (UTC)	Exposure (minutes)	Flux (10^{-5} ph cm^{-2}s^{-1})	TS	ΔTS	Model	Photon Index	Cutoff Energy (MeV)	Proton index
2017-09-10 17:33 - 17:58	24	76.4 ± 1.9	6112	469	Exp	-0.70 $\pm$ 0.30	248 $\pm$ 49	3.30 ± 0.06
2017-09-10 19:03 - 19:39	36	88.3 ± 1.3	16954	1819	Exp	-0.02 $\pm$ 0.07	140 $\pm$ 5	3.70 ± 0.05
2017-09-10 20:44 - 21:08	24	35.8 ± 1.3	2311	276	Exp	0.07 $\pm$ 0.22	117 $\pm$ 11	4.18 ± 0.14
2017-09-10 22:13 - 22:49	36	15.0 ± 0.5	2559	315	Exp	0.35 $\pm$ 0.22	91 $\pm$ 8	4.67 ± 0.16
2017-09-10 23:54 - 00:18	24	5.6 ± 0.5	310	68	Exp	2.03 $\pm$ 0.84	55 $\pm$ 11	4.9 ± 0.4
2017-09-11 01:23 - 02:00	36	2.38 ± 0.22	284	55	Exp	1.69 $\pm$ 0.83	48 $\pm$ 10	6.0 ± 0.5
2017-09-11 03:05 - 03:29	24	1.39 ± 0.28	59	12	Exp	1.00 $\pm$ 1.58	70 $\pm$ 34	5.0 ± 1.0
2017-09-11 04:34 - 05:11	37	0.49 ± 0.11	43	2	PL	-2.65 $\pm$ 0.24	-	-

Table 2:: Maximum likelihood results for each `SunMonitor` observing time window associated with a solar flare detected by the *Fermi*-LAT. Some flares are detected in more than one time window. The horizontal lines separate the flares. The columns are the start date and time of the observing window (reported in UTC), the exposure of the time window, the flux >100 MeV integrated over the observing time window, the TS value for the simple power-law model fit, the ΔTS between the power-law and the power-law with exponential cutoff fit, the model with higher TS value, the photon index from the best fit model, the cutoff energy value (for the cases where the exponential cutoff model best fits the data), best proton index (from fit to the data with pion templates) for the cases where the curved model best describes the data.

Name	Start (UTC)	Duration (sec)	Flux (30 MeV – 10 GeV)	Flux (100 MeV – 10 GeV)	Proton Index	GOES class	SunMonitor detected
FLSF 2010-06-12	2010-06-12 00:55:49	30	446 ± 35	191 ± 12	6.0 ± 0.4	M2.0	NO
FLSF 2011-08-09	2011-08-09 08:01:51	250	31.20 ± 0.24	13.02 ± 0.22	5.68 ± 0.13	X6.9	YES
FLSF 2011-09-06	2011-09-06 22:18:07	100	54.0 ± 1.4	16.6 ± 1.1	3.2 ± 0.4	X2.1	YES
FLSF 2011-09-24	2011-09-24 09:35:53	100	65.2 ± 1.7	0.43 ± 0.07	3.2 ± 0.4	X1.9	YES
FLSF 2012-06-03	2012-06-03 17:53:20	20	111 ± 5	50 ± 5	6.0 ± 1.5	M3.3	YES
FLSF 2012-08-06	2012-08-06 04:36:01	30	205 ± 5	1.79 ± 0.12	6.0 ± 1.5	M1.6	NO
FLSF 2012-10-23	2012-10-23 03:15:33	20	$(3.08 \pm 0.27) \times 10^3$	105 ± 20	6.0 ± 1.5	X1.8	YES
FLSF 2013-10-25b	2013-10-25 20:56:52	10	38.9 ± 1.0	1.13 ± 0.09	6.0 ± 1.5	M1.9	NO
FLSF 2013-10-28a	2013-10-28 01:59:15	70	0.450 ± 0.035	$< 3 \times 10^{-3}$	6.0 ± 1.5	X1.0	NO
FLSF 2013-10-28b	2013-10-28 04:37:48	50	25.9 ± 1.3	0.0029 ± 0.0016	6.0 ± 1.5	M5.1	NO
FLSF 2013-10-28d	2013-10-28 20:54:47	50	9.8 ± 0.6	0.33 ± 0.05	6.0 ± 1.5	M1.5	NO
FLSF 2014-02-25	2014-02-25 00:44:47	400	1407 ± 25	631 ± 26	6.0 ± 0.7	X4.9	YES
FLSF 2014-06-10	2014-06-10 12:47:18	25	6.7 ± 1.3	2.9 ± 1.1	2.2 ± 1.4	X1.5	YES
FLSF 2017-09-10	2017-09-10 15:57:47	325	1060 ± 9	601 ± 7	3.01 ± 0.04	X8.2	YES

Table 3: LLE FLSF catalog results with associated *GOES* X-ray flare. For the cases where the the curved spectrum is preferred we also list the best inferred proton index. The SunMonitor detected column indicates whether the flare was detected by the SunMonitor automatic pipeline. The fluxes are in units of 10^{-5} ph s^{-1} cm^{-2}.

Name	Total duration (hrs)	Flare Type	GOES Start (UT)	GOES Class	CME Speed (km s^{-1})	CME First C2 app. (UT)	SEP Emax (MeV)	HXR Emax (keV)
FLSF 2010-06-12	30*	LLE-Prompt[a]	2010-06-12 00:30	M2.0	486	2010-06-12 01:31	10	1000
FLSF 2011-03-07	15.8 ± 3.1	Delayed	2011-03-07 19:43	M3.7[c]	2125	2011-03-07 20:00	50	>100
FLSF 2011-06-07	6.0 ± 2.2	Delayed	2011-06-07 06:16	M2.5	1255	2011-06-07 06:49	100	100
FLSF 2011-08-04	2.3 ± 0.7	Delayed	2011-08-04 03:41	M9.3	1315	2011-08-04 04:12	100	300
FLSF 2011-08-09	0.87 ± 0.34	Prompt Short-Delayed[a]	2011-08-09 07:48	X6.9	1610	2011-08-09 08:12	100	300
FLSF 2011-09-06	2.0 ± 1.4	LLE-Prompt Short-Delayed[a]	2011-09-06 22:12	X2.1	575	2011-09-06 23:05	100	1000
FLSF 2011-09-07	2.02 ± 0.35	Delayed	2011-09-07 22:32	X1.8	792	2011-09-07 23:05	50[d]	500
FLSF 2011-09-24	1.2 ± 0.7	LLE-Prompt Short-Delayed[a]	2011-09-24 09:21	X1.9	1936	2011-09-24 09:48	50[d]	1000
FLSF 2012-01-23	5.9 ± 1.0	Delayed	2012-01-23 03:38	M8.7	2175	2012-01-23 04:00	100	>100
FLSF 2012-01-27	6.8 ± 1.5	Delayed	2012-01-27 17:37	X1.7	2508	2012-01-27 18:27	605	>100
FLSF 2012-03-05	4.4 ± 1.2	Delayed	2012-03-05 02:30	X1.1	1531	2012-03-05 04:00	40[d]	>100
FLSF 2012-03-07	20.3 ± 0.8	Delayed	2012-03-07 00:02	X5.4[c]	2684[b]	2012-03-07 00:24	605	1000
FLSF 2012-03-09	7.2 ± 1.7	No-Prompt Delayed	2012-03-09 03:22	M6.3	950	2012-03-09 04:26	100[d]	>100
FLSF 2012-03-10	6 ± 4	Delayed	2012-03-10 17:15	M8.4	1296	2012-03-10 18:00	100[d]	>50
FLSF 2012-05-17	2.6 ± 0.5	Delayed	2012-05-17 01:25	M5.1	1582	2012-05-17 01:48	605	>100
FLSF 2012-06-03	1.9 ± 1.5	LLE-Prompt Short-Delayed[a]	2012-06-03 17:48	M3.3	605	2012-06-03 18:12	-	100
FLSF 2012-07-06	1.27 ± 0.35	Delayed	2012-07-06 23:01	X1.1	1828	2012-07-06 23:24	100	-
FLSF 2012-08-06	30*	LLE-Prompt[a]	2012-08-06 04:33	M1.6	198	2012-08-06 05:12	-	100
FLSF 2012-10-23	1.9 ± 0.5	LLE-Prompt Delayed[a]	2012-10-23 03:13	X1.8	-		-	1000
FLSF 2012-11-13	0.041 ± 0.006	Prompt	2012-11-13 01:58	M6.0	851	2012-11-13 02:24	-	100
FLSF 2012-11-27	0.166 ± 0.025	Prompt Short-Delayed	2012-11-27 15:52	M1.6	-		-	500
FLSF 2013-04-11	0.38 ± 0.27	No-Prompt Short-Delayed	2013-04-11 06:55	M6.5	861	2013-04-11 07:24	100	100
FLSF 2013-05-13a	4.0 ± 1.3	Delayed	2013-05-13 01:53	X1.7	1270	2013-05-13 02:00	60	>300
FLSF 2013-05-13b	6.1 ± 2.2	Delayed	2013-05-13 15:48	X2.8	1850	2013-05-13 16:07	60	800
FLSF 2013-05-14	5.9 ± 0.5	No-Prompt Delayed	2013-05-14 00:00	X3.2	2625	2013-05-14 01:25	60	500

Continued on next page

Name	Total duration (hrs)	Flare Type	GOES Start (UT)	GOES Class	CME Speed (km s^{-1})	CME First C2 app. (UT)	SEP Emax (MeV)	HXR Emax (keV)
FLSF 2013-05-15	3.5 ± 0.5	No-Prompt Delayed	2013-05-15 01:25	X1.2	1366	2013-05-15 01:48	50	100
FLSF 2013-10-11	0.38 ± 0.32	BTL Short-Delayed	2013-10-11 07:01	M4.9*	1200	2013-10-11 07:24	60	10
FLSF 2013-10-25a	1.4 ± 0.5	Delayed	2013-10-25 07:53	X1.7	587	2013-10-25 08:12	60	300
FLSF 2013-10-25b	$10^{\star}$	LLE-Prompt[a]	2013-10-25 20:54	M1.9	-		60[d]	100
FLSF 2013-10-28a	$70^{\star}$	LLE-Prompt[a]	2013-10-28 01:41	X1.0	695	2013-10-28 02:24	-	1000
FLSF 2013-10-28b	$50^{\star}$	LLE-Prompt[a]	2013-10-28 04:32	M5.1	1201	2013-10-28 04:48	-	1000
FLSF 2013-10-28c	1.6 ± 0.6	Delayed	2013-10-28 14:46	M2.7[c]	812	2013-10-28 15:36	60	50
FLSF 2013-10-28d	$50^{\star}$	LLE-Prompt[a]	2013-10-28 20:48	M1.5	771	2013-10-28 21:25	100[d]	100
FLSF 2014-01-06	0.27 ± 0.04	BTL Short-Delayed	2014-01-06 07:40	X3.5*	1402	2014-01-06 08:00	605	6
FLSF 2014-01-07	1.05 ± 0.26	Delayed	2014-01-07 18:04	X1.2	1830	2014-01-07 18:24	100	>20
FLSF 2014-02-25	8.4 ± 1.8	LLE-Prompt Delayed[a]	2014-02-25 00:39	X4.9	2147	2014-02-25 01:25	100	7000
FLSF 2014-06-10	1.9 ± 0.6	LLE-Prompt Delayed[a]	2014-06-10 12:36	X1.5	1469	2014-06-10 13:30	60	1000
FLSF 2014-06-11	0.23 ± 0.17	Short-Delayed	2014-06-11 08:59	X1.0	829	2014-06-11 09:24	-	1000
FLSF 2014-09-01	2.5 ± 1.2	BTL Delayed	2014-09-01 10:58	X2.4*	1901	2014-09-01 11:12	100	100
FLSF 2014-09-10	0.30 ± 0.06	Short-Delayed	2014-09-10 17:21	X1.6	1071[b]	2014-09-10 17:24	100	100
FLSF 2015-06-21	11.5 ± 2.5	Prompt Delayed	2015-06-21 02:04	M2.7[c]	1366	2015-06-21 02:36	10	>50
FLSF 2015-06-25	2.4 ± 1.3	Delayed	2015-06-25 08:02	M7.9	1627	2015-06-25 08:36	10	1000
FLSF 2017-09-06a	0.169 ± 0.025	Prompt	2017-09-06 08:57	X2.2	391	2017-09-06 09:48	-	300
FLSF 2017-09-06b	13.33 ± 0.32	Delayed	2017-09-06 11:53	X9.3[c]	1571	2017-09-06 12:24	100	>300
FLSF 2017-09-10	13.9 ± 1.2	Prompt Delayed[a]	2017-09-10 15:35	X8.2	3163	2017-09-10 16:00	605	3000

Table 4:: Multi-wavelength associations for all the FLSF in this work. Entries with a * indicate that the duration is in seconds and not in hours because these are LLE-only flare detections, [a] indicate that there is also a LLE detection of the flare but the total duration refers to the standard analysis, [b] indicates cases with two CMEs and the CME width is marked H for Halo CMEs, which corresponds to a width of 360°, [c] indicates cases where multiple GOES flares were present, [d] indicates that an increase in the SEP energy channel was present.

Name	Flare Type	Duration (hrs)	CME Speed (km s^{-1})	Width	GOES Class	SEP Emax (MeV)	HXR Emax (keV)	AR	AR pos
FLSF 2011-09-06	Prompt Delayed	0.6	575	H	X2.1	100	1000	11283	N14W18
FLSF 2011-09-07	Delayed	1.9	792	290	X1.8	50‡	500	11283	N14W32
FLSF 2012-01-23	Delayed	5.8	2175	H	M8.7	100	>100	11402	N28W20
FLSF 2012-01-27	Delayed	7.3	2508	H	X1.7	605	>100	11402	N29W86
FLSF 2012-03-05	Delayed	5.4	1531	H	X1.1	40‡	>100	11429	N18E41
FLSF 2012-03-07	Delayed	20.2	2684*	H	X5.4*	605	1000	11429	N17E15
FLSF 2012-03-09	Delayed only	7.3	950	H	M6.3	100‡	>100	11429	N17W13
FLSF 2012-03-10	Delayed	6.0	1296	H	M8.4	100‡	>50	11429	N18W27
FLSF 2013-05-13	Delayed	3.4	1270	H	X1.7	60	>300	11748	N12E67
FLSF 2013-05-13	Delayed	5.4	1850	H	X2.8	60	800	11748	N12E67
FLSF 2013-05-14	Delayed only	6.7	2625	H	X3.2	60	500	11748	N12E67
FLSF 2013-05-15	Delayed only	3.6	1366	H	X1.2	50	100	11748	N11E49
FLSF 2013-10-25	Delayed	1.1	587	H	X1.7	60	300	11882	S08E59
FLSF 2013-10-25	Prompt	0.1	-		M1.9	60‡	100	11882	S08E59
FLSF 2013-10-28	Delayed	1.3	812	H	M2.7*	60	50	11882	S08E21
FLSF 2013-10-28	Prompt	0.3	695	H	X1.0	0	1000	11875	N05W72
FLSF 2013-10-28	Prompt	0.1	1201	315	M5.1	0	1000	11875	N08W72
FLSF 2013-10-28	Prompt	0.1	771	284	M1.5	100‡	100	11875	N07W83
FLSF 2014-06-10	Prompt Delayed	1.8	1469	H	X1.5	60	1000	12087	S19E89
FLSF 2014-06-11	Delayed	0.5	829	130	X1.0	0	1000	12087	S18E57
FLSF 2015-06-21	Prompt Delayed	10.2	1366	H	M2.7*	10	>50	12371	N12E16
FLSF 2015-06-25	Delayed	2.1	1627	H	M7.9	10	1000	12371	N11W45
FLSF 2017-09-06	Prompt	0.3	391	245	X2.2	0	300	12673	S09W42
FLSF 2017-09-06	Delayed	13.3	1571	H	X9.3*	100	>300	12673	S09W42
FLSF 2017-09-10	Prompt Delayed	13.6	3163	H	X8.2	605	3000	12673	S08W88

Table 5: List of FLSFs from similar Active Regions (* indicates several X-ray classes or CMEs during the duration of the γ-ray emission. ‡ indicates the previous presence of SEPs, without this event being an SEP event).

The last column provides the position of the AR in heliographics coordinates.

Date and Time	Helio X (″)	Helio Y (″)	ERR 68 (″)	ERR 95 (″)	AR Number	AR Position	Angular Dist (″)	Relative Dist (95)
2011-09-06 22:11 - 22:47	219	533	139	220	11283	N14W18	382	1.7
2012-03-07 00:40 - 01:20	-562	231	56	84	11429	N17E15	45	0.5
2012-03-07 03:51 - 04:31	-300	342	84	144	11429	N17E15	143	1.0
2012-03-07 07:02 - 07:42	-320	20	126	203	11429	N17E15	331	1.6
2012-03-07 10:14 - 10:54	207	245	291	462	11429	N17E15	707	1.5
2012-07-06 23:20 - 00:08	530	-432	362	586	11515	S18W64	122	0.2
2013-05-14 02:43 - 03:31	-1137	333	314	504	11748	N12E67	279	0.6
2013-10-11 06:56 - 07:39	-930	311	151	263	BTL	N21E103	-	-
2014-02-25 01:09 - 01:29	-933	-347	92	147	11990	S15E65	63	0.4
2014-02-25 04:20 - 04:40	-982	-213	358	574	11990	S15E65	109	0.2
2014-09-01 11:02 - 11:18	-1126	-182	202	322	BTL	N14E126	-	-
2017-09-10 15:52 - 16:28	847	-207	59	95	12673	S08W88	72	0.8
2017-09-10 19:03 - 19:39	1034	-131	104	166	12673	S08W88	168	1.0
2017-09-10 22:13 - 22:49	1139	137	271	443	12673	S08W88	336	0.8

Table 6: Localization results for the FLSFs with 68% error radius $<0.1^{\circ}$. We report the date and detection time window start and stop, LAT >100 MeV emission centroid position in Helio X and Y coordinates, the 68% and 95% error radius (in arcseconds), the AR number and position, the distance of the centroid from the active region, and the ratio of this distance to the 95% error radius.

GOES Start-Stop	GOES Class	CME First appear. (UT)	CME Speed (kms^{-1})	CME Width (°)	LAT Observable	SEP event
2011-02-15 01:44 - 02:06	X2.2	2011-02-15 02:24	669	Halo	X	-
2011-03-09 23:13 - 23:29	X1.5	-	-	-	X	-
2011-09-22 10:29 - 11:44	X1.4	2011-09-22 10:48	1905	Halo	-	SEP
2011-11-03 20:16 - 20:32	X1.9	-	-	-	-	-
2012-07-12 15:37 - 17:30	X1.4	2012-07-12 16:24	843	76	X	SEP
2013-10-25 14:51 - 15:12	X2.1	2013-10-25 15:12	1081	Halo	-	-
2013-10-29 21:42 - 22:01	X2.3	2013-10-29 22:00	1001	Halo	-	-
2013-11-05 22:07 - 22:15	X3.3	2013-11-05 22:36	562	195	-	-
2013-11-08 04:20 - 04:29	X1.1	-	-	-	-	-
2013-11-10 05:08 - 05:18	X1.1	2013-11-10 05:36	682	262	-	-
2013-11-19 10:14 - 10:34	X1.0	2013-11-19 10:36	740	Halo	-	-
2014-03-29 17:35 - 17:54	X1.0	2014-03-29 18:12	528	Halo	-	-
2014-04-25 00:17 - 00:38	X1.3	2014-04-25 00:48	456	296	X	-
2014-06-10 11:36 - 11:44	X2.2	2014-06-10 11:48	925	111	-	-
2014-10-19 04:17 - 05:48	X1.1	2014-10-19 06:12	170	43	-	-
2014-10-22 14:02 - 14:50	X1.6	-	-	-	X	-
2014-10-24 21:07 - 22:13	X3.1	2014-10-24 21:48	184	35	-	-
2014-10-25 16:55 - 18:11	X1.0	2014-10-25 17:36	171	49	-	-
2014-10-26 10:04 - 11:18	X2.0	-	-	-	X	-
2014-10-27 14:12 - 15:09	X2.0	2014-10-27 15:12	170	55	-	-
2014-11-07 16:53 - 17:34	X1.6	2014-11-07 17:12	469	87	-	-
2014-12-20 00:11 - 00:55	X1.8	-	-	-	X	-
2015-03-11 16:11 - 16:29	X2.2	2015-03-11 17:00	240	74	-	-
2015-05-05 22:05 - 22:15	X2.7	2015-05-05 22:24	715	Halo	-	-
2017-09-07 14:20 - 14:55	X1.3	2017-03-09 12:36	223	7	-	-

Table 7: X-class GOES flares not associated with any γ-ray emission above 30 MeV. The *Fermi*-LAT observable column indicates whether the prompt phase of the X-ray flare occurred within a `SunMonitor` time window. The SEP event column indicates the presence of this flare in the Major SEP Event list.

REFERENCES

Abdo, A. A., Ackermann, M., Ajello, M., et al. 2011, ApJ, 734, 116

Abeysekara, A. U., Archer, A., Benbow, W., et al. 2018, ApJ, 866, 24

Ackermann, M., Ajello, M., Allafort, A., et al. 2012a, ApJ, 745, 144

Ackermann, M., Ajello, M., Albert, A., et al. 2012b, ApJS, 203, 4

Ackermann, M., Ajello, M., Albert, A., et al. 2014a, ApJ, 787, 15

Ackermann, M., Ajello, M., Albert, A., et al. 2014b, ApJ, 787, 15

Ackermann, M., Allafort, A., Baldini, L., et al. 2017, ApJ, 835, 219

Ackermann, M., Ajello, M., Baldini, L., et al. 2018, ApJS, 237, 32

Ahnen, M. L., Ansoldi, S., Antonelli, L. A., et al. 2019, MNRAS, 485, 356

Ajello, M., Albert, A., Allafort, A., et al. 2014, ApJ, 789, 20

Ajello, M., Baldini, L., Bastieri, D., et al. 2020, The First Fermi-LAT Solar Flare Catalog Appendix

Arnaud, K. A. 1996, in Astronomical Society of the Pacific Conference Series, Vol. 101, Astronomical Data Analysis Software and Systems V, ed. G. H. Jacoby & J. Barnes, 17

Atwood, W., Albert, A., Baldini, L., et al. 2013, arXiv e-prints, arXiv:1303.3514

Atwood, W. B., Abdo, A. A., Ackermann, M., et al. 2009, ApJ, 697, 1071

Barat, C., Trottet, G., Vilmer, N., et al. 1994, ApJ, 425, L109

Bruel, P., Burnett, T. H., Digel, S. W., et al. 2018, Fermi-LAT improved Pass 8 event selection

Chupp, E. L. 1987, Physica Scripta Volume T, 18, 5

Chupp, E. L., & Ryan, J. M. 2009, Research in Astronomy and Astrophysics, 9, 11

Chupp, E. L., Forrest, D. J., Ryan, J. M., et al. 1982, ApJ, 263, L95

Cliver, E. W., Kahler, S. W., & Vestrand, W. T. 1993, in International Cosmic Ray Conference, Vol. 3, 23rd International Cosmic Ray Conference (ICRC23), Volume 3, 91

De Nolfo, G., Bruno, A., Ryan, J., et al. 2019, Astrophysical Journal, 879, cited By 7

Dennis, B. R. 1988, Sol. Phys., 118, 49

Di Mauro, M., Manconi, S., Zechlin, H. S., et al. 2018, ApJ, 856, 106

Dolan, J. F., & Fazio, G. G. 1965, Reviews of Geophysics, 3, 319

Forrest, D. J., Vestrand, W. T., Chupp, E. L., Rieger, E., & Cooper, J. 1986, Advances in Space Research, 6, 115

Forrest, D. J., Vestrand, W. T., Chupp, E. L., et al. 1985, in International Cosmic Ray Conference, Vol. 4, 19th International Cosmic Ray Conference (ICRC19), Volume 4, 146

Hurford, G. J., Krucker, S., Lin, R. P., et al. 2006, ApJ, 644, L93

Jin, M., Petrosian, V., Liu, W., et al. 2018, ApJ, 867, 122

Kanbach, G., Bertsch, D. L., Fichtel, C. E., et al. 1993, A&AS, 97, 349

Kocharov, L., Pesce-Rollins, M., Laitinen, T., et al. 2020, ApJ, 890, 13

Lin, R. P., & Rhessi Team. 2003, Advances in Space Research, 32, 1001

Linden, T., Zhou, B., Beacom, J. F., et al. 2018, Phys. Rev. Lett., 121, 131103

Mattox, J. R., Bertsch, D. L., Chiang, J., et al. 1996, ApJ, 461, 396

Mazziotta, M. N., Luque, P. D. L. T., Di Venere, L., et al. 2020, Phys. Rev. D, 101, 083011

Meegan, C., Lichti, G., Bhat, P. N., et al. 2009, ApJ, 702, 791

Moskalenko, I. V., Porter, T. A., & Digel, S. W. 2006, ApJ, 652, L65

Murphy, R. J., Dermer, C. D., & Ramaty, R. 1987, ApJS, 63, 721

Nitta, N. V., Aschwanden, M. J., Boerner, P. F., et al. 2013, Sol. Phys., 288, 241

Omodei, N., Pesce-Rollins, M., Longo, F., Allafort, A., & Krucker, S. 2018, ApJ, 865, L7

Orlando, E., & Strong, A. W. 2007, Ap&SS, 309, 359

—. 2008, A&A, 480, 847

Pesce-Rollins, M., Omodei, N., Petrosian, V., et al. 2015, ApJ, 805, L15

Poluianov, S. V., Usoskin, I. G., Mishev, A. L., Shea, M. A., & Smart, D. F. 2017, Solar Physics, 292, 176

Reames, D. V. 1995, Advances in Space Research, 15, 41

Ryan, J. M. 2000, Space Sci. Rev., 93, 581

Ryan, J. M., & Lee, M. A. 1991, ApJ, 368, 316

Sakurai, T. 2008, The Hinode Mission (Springer)

Seckel, D., Stanev, T., & Gaisser, T. K. 1991, ApJ, 382, 652

Shih, A. Y., Lin, R. P., & Smith, D. M. 2009, ApJ, 698, L152

Shrivastava, P. K., & Singh, N. 2005, Chinese Journal of Astronomy and Astrophysics, 5, 198

Thompson, D. J., , et al. 1993, ApJS, 86, 629

Trottet, G., Vilmer, N., Barat, C., et al. 1998, A&A, 334, 1099

Vestrand, W. T., & Forrest, D. J. 1993, ApJ, 409, L69

Vianello, G., Lauer, R. J., Younk, P., et al. 2015, arXiv e-prints, arXiv:1507.08343

Vilmer, N. 1987, Hard X-ray Emission Processes in Solar Flares (Dordrecht: Springer Netherlands), 207–223

Vilmer, N., MacKinnon, A. L., & Hurford, G. J. 2011, Space Sci. Rev., 159, 167

Vilmer, N., MacKinnon, A. L., Trottet, G., & Barat, C. 2003, A&A, 412, 865

Vilmer, N., Trottet, G., Barat, C., et al. 1999, A&A, 342, 575

Wood, M., Caputo, R., Charles, E., et al. 2017, in International Cosmic Ray Conference, Vol. 301, 35th International Cosmic Ray Conference (ICRC2017), 824

This manuscript was prepared with the AAS LaTeX macros v5.2.